Glide-resolved photoemission spectroscopy: Measuring topological invariants in nonsymmorphic space groups

A. Alexandradinata,[1,*] Zhijun Wang,[2,3] B. Andrei Bernevig,[4,5,6] and Michael Zaletel[4]
[1]*Department of Physics and Institute for Condensed Matter Theory, University of Illinois at Urbana-Champaign, Urbana, Illinois 61801, USA*
[2]*Beijing National Laboratory for Condensed Matter Physics, and Institute of Physics, Chinese Academy of Sciences, Beijing 100190, China*
[3]*University of Chinese Academy of Sciences, Beijing 100049, China*
[4]*Department of Physics, Princeton University, Princeton New Jersey 08544, USA*
[5]*Physics Department, Freie Universitat Berlin, Arnimallee 14, 14195 Berlin, Germany*
[6]*Max Planck Institute of Microstructure Physics, 06120 Halle, Germany*

(Received 22 April 2019; accepted 4 June 2020; published 29 June 2020; corrected 7 July 2020)

The two classes of 3D, time-reversal-invariant insulators are known to subdivide into four classes in the presence of glide symmetry. Here, we extend this classification of insulators to include glide-symmetric Weyl metals and find a finer $\mathbb{Z}_4 \oplus \mathbb{Z}$ classification. We further elucidate the smoking-gun experimental signature of each class in the photoemission spectroscopy of surface states. Measuring the $\mathbb{Z}_4$ topological invariant by photoemission relies on identifying the glide representation of the initial Bloch state before photoexcitation—we show how this is accomplished with relativistic selection rules, combined with standard spectroscopic techniques to resolve both momentum and spin. Our method relies on a spin-momentum locking that is characteristic of all glide-symmetric solids (inclusive of insulators and metals in trivial and topological categories). As an orthogonal application, given a glide-symmetric solid with an ideally symmetric surface, we may utilize this spin-momentum locking to generate a source of *fully* spin-polarized photoelectrons, which have diverse applications in solid-state spectroscopy. Our *ab initio* calculations predict Ba_2Pb, stressed Na_3Bi, and KHgSb to realize all three, nontrivial insulating phases in the $\mathbb{Z}_4$ classification.

DOI: 10.1103/PhysRevB.101.235166

Despite exhaustive theoretical classifications and modeling of topological insulators and semimetals over hundreds of space groups [1–13], there have been fewer material realizations, and far fewer translations of abstract topological invariants into experimental observables. This work provides the translation for a new class of topological solids protected by nonsymmorphic crystalline symmetries [1–3,14–22]—symmetries that unavoidably translate space by a rational fraction of the lattice period [23]. A case in point is glide-symmetric KHgSb which is invariant under reflection composed with half a lattice translation; KHgSb represents a nonsymmorphic topological insulator [1,2] with hourglass-fermion surface states that have been experimentally confirmed [24,25].

From the perspective of topological classification of band insulators, the two well-known classes [26–29] of 3D, time-reversal-invariant insulators subdivide into four classes [3,30] in the presence of glide symmetry. Indeed, while the $\mathbb{Z}_2$ classification in the absence of glide symmetry corresponds to the number (even vs odd) of Dirac fermions on the surface of an insulator, glide symmetry further assigns to each Dirac fermion a "chirality" which enriches the classification to $\mathbb{Z}_4$. To appreciate this, consider a glide-invariant cross section (in $\boldsymbol{k}$ space) of a Dirac fermion, as illustrated in Fig. 1(a); each Bloch state (with wave vector in this cross section) carries a glide eigenvalue which takes on one of two values (denoted as $\Delta_\pm$). The chirality of the Dirac fermion is defined to be positive (resp. negative) if the right-moving mode has eigenvalue Δ_+ (resp. Δ_-), as illustrated in Fig. 1(b) [resp. (c)]. Two fermions with positive chirality [first panel of Fig. 1(d)] represent a nontrivial insulator whose surface-band dispersion resembles an hourglass [second panel of Fig. 1(d)] [1,2]. This same dispersion can be deformed to two fermions with negative chirality [sequenced panels in Fig. 1(d)] while preserving surface states at any energy in the bulk gap (as illustrated in third column of Fig. 3) [31], this provides a heuristic argument for the $\mathbb{Z}_4$ classification of glide-symmetric insulators.

One of our aims is to extend this classification to describe glide-symmetric solids—inclusive of insulators and topological metals—and to further elucidate the smoking-gun experimental signature of each class of solids. As described in Sec. II, the classification of topological solids is $\mathbb{Z}_4 \oplus \mathbb{Z}$, with $\mathbb{Z}$ corresponding to the net number of Weyl points in a symmetry-reduced quadrant of the Brillouin zone. Each class of $\mathbb{Z}_4 \oplus \mathbb{Z}$ can be experimentally distinguished through (a) the holonomy of bulk Bloch functions over noncontractible loops of the Brillouin torus, as well as through (b) the photoemission spectroscopy [32,33] (PES) of surface states, as discussed in Sec. IV. (a) and (b) are related by the bulk-boundary correspondence [2,34,35] of topological insulators and metals.

We propose that our theory is materialized in Sec. III by Ba_2Pb, uniaxially-stressed Na_3Bi, and KHgSb; they respectively fall into the classes: $(\chi^+ \in \mathbb{Z}_4, \mathcal{C} \in \mathbb{Z}) = (3, 0)$, (1,0), and (2,0). For the Dirac semimetal Na_3Bi, we consider a stress that preserves the glide symmetry but destabilizes the Dirac crossings between conduction and valence bands [36],

---

[*] Corresponding author: aalexan7@illinois.edu

thus inducing a transition from a Dirac semimetal (with space group D_{6h}^4) to a $\chi^+ = 1$ topological insulator (with nonsymmorphic space group 63); such a transition is deducible using the methods of topological quantum chemistry [21]. While it is known that Ba_2Pb and gapped Na_3Bi belong to the same nontrivial phase under the $\mathbb{Z}_2$ time-reversal-symmetric classification [36,37], here we propose that they are distinct phases in the $\mathbb{Z}_4$ glide-symmetric classification and may be distinguished by photoemission spectroscopy.

Measuring the $\mathbb{Z}_4$ topological invariant through photoemission relies on identifying the glide eigenvalues ($\Delta_\pm$) of Bloch states before they are photoexcited [cf. Figs. 3(c)–3(h)]. By combining angle-resolved PES with dipole selection rules [38,39], it is known how to determine the integer-spin representation of glide for solids without spin-orbit coupling [40,41]. However, this method is insufficient to determine half-integer-spin representations of glide for spin-orbit-coupled solids, which are the subject of this work. Here, we show that spin- and angle-resolved PES, which was not addressed during the previous works [38–42], provides the missing ingredient to identify glide eigenvalues—and therefore the $\mathbb{Z}_4$ index—in spin-orbit-coupled solids.

Our proposed method relies on photoexciting a glide-invariant Bloch state with linearly-polarized radiation. The excited photoelectron is emitted (into vacuum) as a quantum superposition of plane waves, with wave vectors differing only by reciprocal vectors of the solid (with a surface). The wave vectors lying within the glide-invariant plane form a fan of rays that is illustrated in Fig. 1(e). If the polarization vector of the incoming radiation lies orthogonal to the glide-invariant plane, then photoelectrons on any pair of adjacent rays are fully spin polarized in opposite directions—normal and antinormal to the glide-invariant plane. As we will demonstrate in Sec. V, this perfect spin-momentum locking of the photoelectron is a *general* manifestation of spin-orbit coupling in all glide-symmetric solids (trivial or topological, insulating or metallic); the generalization to mirror-symmetric solids will also be discussed. As an orthogonal application of this locking, one may generate a fully spin-polarized photoelectronic current (photocurrent, in short) by isolating one of the rays in Fig. 1(e) using standard angle-resolved PES techniques. The potential applications to solid-state spectroscopy are discussed in Sec. VI.

The reader who is solely interested in this spin-momentum locking (and how it is utilized to resolve glide eigenvalues in PES) may jump straight to Sec. V, which has been designed to be a self-contained exposition. In Sec. VI, we elaborate on our proposal to generate spin-polarized photocurrents, as well as compare it with existing theoretical proposals. We also summarize our main results and discuss further experimental implications.

I. PRELIMINARIES ON NONSYMMORPHIC SPACE-GROUP REPRESENTATIONS

Throughout this work, we focus on spin-orbit-coupled solids whose space groups contain (minimally) the operations of time reversal and glide. We adopt a Cartesian coordinate system (x, y, z), with corresponding unit directional vectors $(\vec{\boldsymbol{x}}, \vec{\boldsymbol{y}}, \vec{\boldsymbol{z}})$, such that the glide symmetry (denoted as g_x) maps $(x, y, z) \to (-x, y + R_2/2, z)$, where R_2 is the lattice period in the $\vec{\boldsymbol{y}}$ direction. That is, g_x is the composition of two commuting operations: a reflection (r_x) that inverts x and a translation by half a lattice period in $\vec{\boldsymbol{y}}$. This implies g_x^2 is the product of a full lattice translation and r_x^2; the latter acts on spinor wave functions like a 2π rotation, i.e., it produces a -1 phase factor.

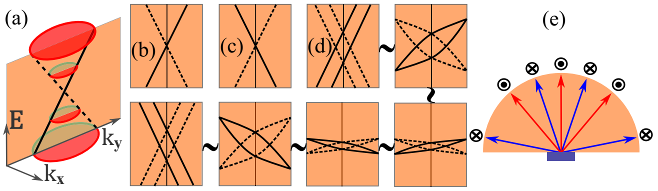

FIG. 1. (a) Band dispersion of a Dirac fermion. The glide-invariant cross section of a Dirac cone corresponds to a right- and left-moving mode, as indicated by two intersecting black lines. A solid (resp. dashed) line corresponds to the glide eigenvalue being Δ_+ (resp. Δ_-). (b)–(d) Glide-invariant cross sections of a variety of surface states. (e) A glide-invariant Bloch state (localized to the rectangular sample) absorbs a photon and is emitted as a superposition of plane waves traveling in several directions, as illustrated by the fan of arrows parallel to the glide-invariant plane (colored orange); neighboring arrows differ by a reciprocal vector of the solid. For blue arrows, the photoelectron spin points into the board, and for red it points out.

Let us review the irreducible half-integer-spin representations of glide and discrete translational symmetries. The irreducible representations of translations are Bloch states labeled by a crystal wave vector $\boldsymbol{k} = (k_x, k_y, k_z)$ in the first Brillouin zone (BZ). Since g_x maps $\boldsymbol{k} \to (-k_x, k_y, k_z)$, the glide-invariant Bloch functions lie in two cuts of the BZ: The $k_x = 0$ cut through the BZ center will be referred to as the central glide plane, and the $k_x = \pi/a_1$ plane (with $2\pi/a_1$ a reciprocal period in the $\vec{\boldsymbol{x}}$ direction) will be referred to as the off-center glide plane. As illustrated in Fig. 2(a), the positive-k_y halves of the central and off-center glide plane are labeled by c and a, respectively.

Let $\hat{g}_x$ be an operator representing g_x on spinor wave functions. The action of $\hat{g}_x^2$ on a glide-invariant spinor Bloch function produces a phase $-e^{-ik_yR_2}$, hence the possible eigenvalues of $\hat{g}_x$ fall into two branches of $\Delta_\pm(k_y) := \pm i \exp[-ik_yR_2/2]$. A Bloch state with glide eigenvalue $\Delta_\pm(k_y)$ is said to be in the $\Delta_\pm(k_y)$ representation; we will use 'eigenvalue' and 'representation' interchangeably. The typical energy band dispersions along two glide- and time-reversal-invariant lines are illustrated in Figs. 2(c) and 2(d); each solid black line (resp. dashed black line) indicates a band in the Δ_+ (resp. Δ_-) representation; this convention is adopted in all figures. The symmetry-enforced band connectivities in Figs. 2(c) and 2(d) are further explained in Appendix A 2.

II. CLASSIFICATION OF NONSYMMORPHIC TOPOLOGICAL SOLIDS

A. Zak-phase expression of the $\mathbb{Z}_4$ invariant

In Ref. [3], a topological invariant $\chi^+ \in \mathbb{Z}_4 := \{0, 1, 2, 3\}$—expressible as an integral of the Berry connection

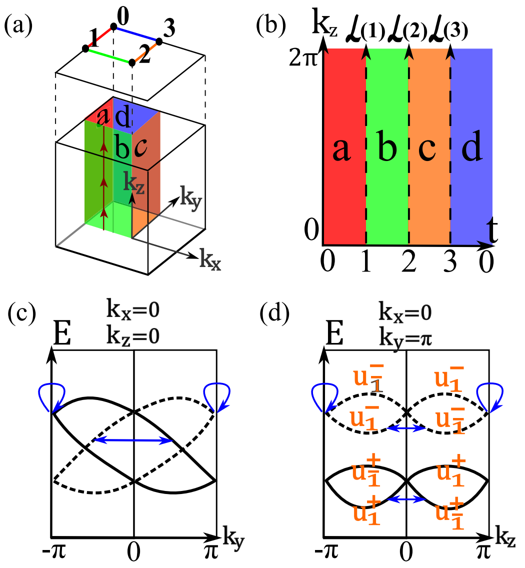

FIG. 2. (a) 3D Brillouin zone (BZ) of glide-symmetric solids. For certain nonsymmorphic space groups which contain glide symmetry (e.g., D_{6h}^4, the space group of KHgSb), their BZs are not cubic, and (a) should be understood as a modified BZ corresponding to a nonprimitive real-space unit cell; further details may be found in Appendix C. We will define topological invariants on a 2D subregion that combines four colored faces, which are labeled *abcd* and parametrized in (b). Red (*a*) and orange (*c*) faces are glide invariant. (c),(d) For noncentrosymmetric space groups, we illustrate typical energy-band dispersions on two glide- and time-reversal-invariant lines, the first at fixed $k_x = k_z = 0$ and the second at fixed $k_x = 0, k_y = \pi$ ($R_2 = 1$). Solid and dashed lines, respectively, indicate bands in the Δ_+ and Δ_- representations, with corresponding glide eigenvalues $\Delta_\pm(k_y) = \pm i \exp[-ik_y/2]$. Arrows indicate states related by time reversal.

and curvature—was introduced by Shiozaki, Sato, and Gomi to classify glide-invariant topological insulators. The same invariant provides a *partial* classification of glide-invariant topological (semi)metals, so long as touchings—between conduction and valence bands—occur away from the bent, 2D subregion colored in Fig. 2(a). This subregion resembles the face of a rectangular pipe (with its ends identified due to the periodicity of the BZ). The faces of the cylinder are denoted *a*, *b*, *c*, and *d*, with *c* and *a* belonging to the central and off-center glide planes, respectively. In the absence of additional point-group symmetry that might restrict conduction-valence touchings to *abcd* [43], we may assume in the generic situation that such touchings occur elsewhere.

Let us present an equivalent reformulation of the $\mathbb{Z}_4$ invariant (χ^+) through the matrix holonomy of multiband Bloch functions over the Brillouin torus. The comparative advantages of our formulation are that the eigenvalues of the holonomy matrix, as represented by the graphs in Fig. 3: (i) are potentially measurable by interference experiments [44,45], (ii) are directly relatable to surface states through the bulk-boundary correspondence [2,34,35], as will be elaborated below, and (iii) are efficiently computed from tight-binding models and first-principles calculations [46–48]. In this section, we will explain how the aforementioned graphs

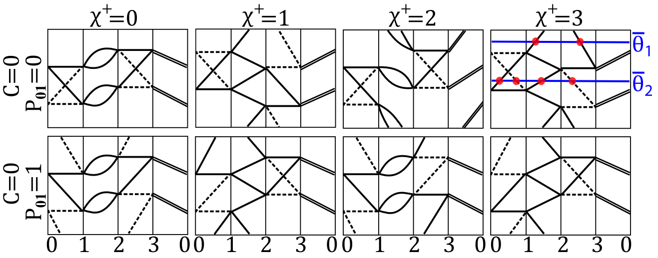

FIG. 3. Classification of glide-symmetric insulators by a strong $\mathbb{Z}_4$ invariant (χ^+) and a weak $\mathbb{Z}_2$ invariant ($\mathcal{P}_{01}$). The vertical axis has the double interpretation as a Berry-Zak phase $\theta \in [0, 2\pi]$ or as the energy of a surface-localized state (that interpolates between conduction and valence bands). The integer labels in the horizontal axis correspond to high-symmetry wave vectors illustrated in Figs. 2(a) and 2(b). Bands are doubly degenerate along the high-symmetry line 30 and glide invariant along 01 and 23 only.

are attained and describe an elementary method to identify χ^+ from these graphs. The proof of equivalence between our holonomy formulation of χ^+ and the Shiozaki-Sato-Gomi formulation is postponed to Appendix B.

To begin, let us consider the parallel transport of Bloch states in the *z* direction, i.e., the wave number k_z of a Bloch state is advanced by a reciprocal period, while the *reduced wave vector* $\boldsymbol{k}_\parallel = (k_x, k_y)$ is fixed. We consider a family of noncontractible loops within *abcd* [Fig. 2(a)]; this family is parameterized by $t \in [0, 4]$ with $4 \equiv 0$ [Fig. 2(b)]. A Bloch state that is parallel transported over a loop does not necessarily return to its initial state; the mismatch between initial and final states is represented by a holonomy matrix $\mathcal{W}$ in the space of occupied bands (numbering n_{occ}). $\mathcal{W}$ is known as the Wilson loop of the non-Abelian Berry gauge field [49], and its unimodular eigenvalues $\{\exp[i\theta_j(t)] | j = 1, 2, \ldots, n_{\text{occ}}; t \in [0, 4]\}$ are the Zak phase factors. In analogy with energy bands, we may refer to $\theta_j(t)$ as the dispersion of a 'Zak band' with band index *j*. For $t \in [0, 1]$ and [2,3] (which correspond to the glide-invariant faces *a* and *c*), $\mathcal{W}$ block diagonalizes into two $n_{\text{occ}}/2$-by-$n_{\text{occ}}/2$ blocks [50], corresponding to the two representations ($\Delta_\pm$) of glide; we may therefore label the Zak bands as $\{\theta_j^\pm\}_{j=1}^{n_{\text{occ}}/2}$.

As proven in Appendix B, the $\mathbb{Z}_4$ topological invariant is expressible as:

$$\chi^\pm = \frac{1}{\pi}\sum_{j=1}^{n_{\text{occ}}/2}\left[\theta_j^\pm\Big|_0 - \theta_j^\pm\Big|_3 + \int_0^1 d\theta_j^\pm + \int_2^3 d\theta_j^\pm\right] + \frac{1}{2\pi}\sum_{j=1}^{n_{\text{occ}}}\int_1^2 d\theta_j. \qquad (1)$$

For this expression to be well-defined modulo four, we choose that (i) θ_j is smooth with respect to *t* over [1,2], (ii) $\theta_j^\pm$ is smooth over [0,1] and [2,3], and (iii) $\theta_j^\pm(t)$ are pairwise degenerate at $t = 0$ and 3. To clarify (iii), for any $j \in \{1, \ldots, n_{\text{occ}}/2\}$, there exists $j' \in \{1, \ldots, n_{\text{occ}}/2\}$ such that $j \neq j'$, $\theta_j^\pm(0) = \theta_{j'}^\pm(0)$, and $\theta_j^\pm(3) = \theta_{j'}^\pm(3)$.

From Eq. (1), we derive the simplest way to identify $\chi^\pm$ from the Zak-phase spectrum: For an arbitrarily chosen $\bar{\theta}$, draw a constant-$\bar{\theta}$ reference line (as illustrated in blue in the rightmost column of Fig. 3) and consider its intersections with Zak bands (indicated by red dots). For each intersection occurring at $t \in (1,2)$, we calculate the sign of the velocity $d\theta/dt$ and sum this quantity over all intersections [over $t \in (1,2)$] to obtain $\mathcal{S}_{12}(\bar\theta)$; for $t \in [0,1]$ and [2,3], we consider only intersections with Zak bands in the $\Delta_\pm$ representation, and we similarly sum over sgn$[d\theta/dt]$ to obtain $\mathcal{S}^{\pm}_{01}(\bar\theta)$ and $\mathcal{S}^{\pm}_{23}(\bar\theta)$, respectively. The following *weighted* sum of $\mathcal{S}^{\pm}_{ij}$ and $\mathcal{S}_{12}$,

$$\mathcal{S}^{\pm}(\bar\theta) = 2\mathcal{S}^{\pm}_{01}(\bar\theta) + \mathcal{S}_{12}(\bar\theta) + 2\mathcal{S}^{\pm}_{23}(\bar\theta), \tag{2}$$

satisfies that $(\mathcal{S}^{\pm}(\bar\theta_1) - \mathcal{S}^{\pm}(\bar\theta_2))/4 \in \mathbb{Z}$ for any two reference lines at constant $\bar\theta_1$ and $\bar\theta_2$, e.g., compare $\mathcal{S}^{+}(\bar\theta_1) = 2(0) + 1 + 2(-1) = -1$ (upper blue line in Fig. 3) with $\mathcal{S}^{+}(\bar\theta_2) = 2(+1) + 1 + 2(0) = 3$ (lower blue line). Equivalently stated, if we henceforth view $\mathcal{S}^{\pm}(\bar\theta)$ as an element in $\mathbb{Z}_4$, then this quantity becomes independent of $\bar\theta$. By also viewing $\chi^{\pm}$ as a $\mathbb{Z}_4$ quantity, we may identify $\mathcal{S}^{\pm} \equiv \chi^{\pm}$ by comparing Eq. (1) with Eq. (2). To clarify, $\equiv$ denotes an identity between two equivalence classes in $\mathbb{Z}_4$.

B. Extended classification of glide-symmetric topological solids

We now demonstrate that $\chi^{+} \equiv -\chi^{-}$ for insulators, while this is not necessarily true for Weyl metals. We are considering time-reversal- and glide-symmetric Weyl metals that occur only in noncentrosymmetric space groups [51,52]. Such metals may be characterized by counting the net number of Weyl nodes in the open Brillouin-zone quadrant $\mathcal{O}$ surrounded by (but not including) the faces *abcd* [Fig. 3(a)]. $\mathcal{O}$ resembles the interior of a rectangular pipe, and its properties determine those of the other three quadrants owing to g_x and time-reversal symmetry. Each Weyl node has a signed charge (q) corresponding to whether it is a source ($q = +1$) or sink ($q = -1$) of the Berry field strength; the net charge within $\mathcal{O}$ is quantified by the bent Chern number ($\mathcal{C}$) [53], which may be formulated as the net winding of $\theta(t)$ for $t \in [0,4]$, or equivalently as the summation of sign$[d\theta/dt]$, over all intersections with a constant-$\bar\theta$ reference line. The sum is carried out over all bands indiscriminate of their symmetry representations, therefore

$$\mathcal{C} = \tfrac{1}{2}[\mathcal{S}^{+}(\bar\theta) + \mathcal{S}^{-}(\bar\theta)] + \mathcal{S}_{30}(\bar\theta). \tag{3}$$

To clarify, $\mathcal{S}_{30}$ here is the summation of sign$[d\theta/dt]$ over the interval $t \in (3,4)$, which corresponds to the blue line 30 in Fig. 2(a); $\mathcal{S}_{30}$ must be even because Zak bands are doubly degenerate due to $g_x T$ symmetry [1]. While each of $\mathcal{S}^{\pm}$ and $\mathcal{S}_{30}$ may individually depend on the choice of reference line, their weighted sum ($\mathcal{C}$) does not. Applying that $2\mathcal{S}_{30}$ is an integer multiple of four, and the relation $\mathcal{S}^{\pm} \equiv \chi^{\pm}$ from the previous paragraph, we derive

$$(\chi^{+} + \chi^{-}) \equiv 2\mathcal{C} \mod 4, \tag{4}$$

which implies a $\mathbb{Z} \oplus \mathbb{Z}_4$ classification of glide-symmetric solids, inclusive of metals and insulators. To recapitulate, $\mathbb{Z}$ counts the net number of Weyl points in a symmetry-reduced quadrant of the BZ. Representative examples for $\mathcal{C} = 1$ and 2 are illustrated in Fig. 4.

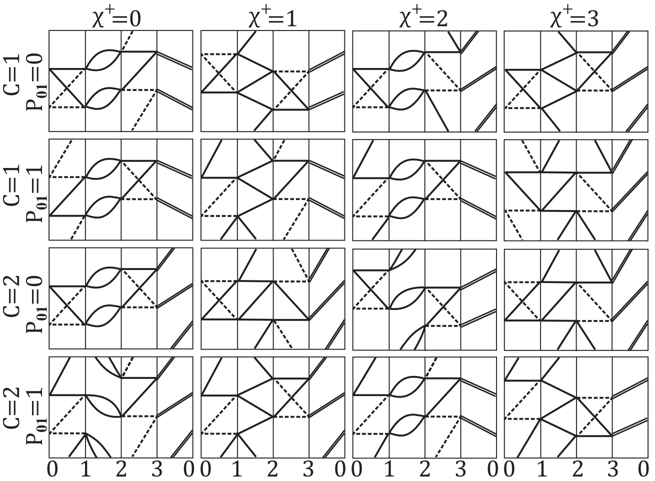

FIG. 4. Topological classification of glide-symmetric metals with $\mathcal{C} \in \mathbb{Z}$ and $\chi^{+} \in \mathbb{Z}_4$. A finer classification is possible with the introduction of $\mathcal{P}_{01} \in \mathbb{Z}_2$—a weak topological invariant that is defined in Sec. III. Note that $\chi^{+} \in \{0,1,2,3\}$ should be viewed as the mod-four equivalence class of the quantity defined in Eq. (1) or equivalently in Eq. (2).

C. Surface states of nonsymmorphic topological solids

We now extend our discussion to the physics of surface states. We terminate the solid in the z direction by introducing a surface that is symmetric under glide and discrete translations in the xy plane. We further assume that the surface is clean and does not undergo a symmetry-breaking reconstruction. So long as the above-stated symmetries are preserved, the exact termination of the surface (including relaxation effects) is not essential to our discussion—we are concerned only with topological aspects of the surface states.

The translational symmetry implies the existence of a surface Brillouin zone (sBZ) that is parametrized by the wave vector $\boldsymbol{k}_{\parallel}$; recall that $(\boldsymbol{k}_{\parallel}, k_z)$ parametrizes the bulk Brillouin zone (bBZ) of a solid that is periodic in three directions. Energy bands whose wave function is localized to the surface shall be referred to as surface bands. Such surface bands can only exist at $\boldsymbol{k}_{\parallel} \in s$BZ for which there is a bulk energy gap at the reduced wave vector $\boldsymbol{k}_{\parallel}$; in particular, they cannot exist at $\boldsymbol{k}_{\parallel} \in s$BZ if a Weyl point lies at $(\boldsymbol{k}_{\parallel}, k_z) \in b$BZ for some k_z.

Our previous discussion of Zak bands may be related to surface bands by the bulk-boundary correspondence. This correspondence states that the connectivity of Zak bands (over the reduced wave vector $\boldsymbol{k}_{\parallel}$) is topologically equivalent to the connectivity of surface bands (over the surface wave vector $\boldsymbol{k}_{\parallel}$) [2,34,35]. We shall only concern ourselves with the connectivity over on the high-symmetry lines 01, 12, 23, 30 in sBZ [see Fig. 3(a)]; they are, respectively, the projections of the faces a, b, c, and d in bBZ. Given our assumption that Weyl points (if they exist) lie away from *abcd*, surface bands potentially exist along 01230, and their connectivity is then well defined.

$\chi^{\pm}$ may be identified by considering intersections between surface bands (over 0123) and a constant-energy reference line (e.g., the Fermi level). This reference line is chosen so as not to intersect any bulk bands; $\mathcal{S}_{12}$ and $\mathcal{S}^{\pm}_{ij}$ in Eq. (2) are

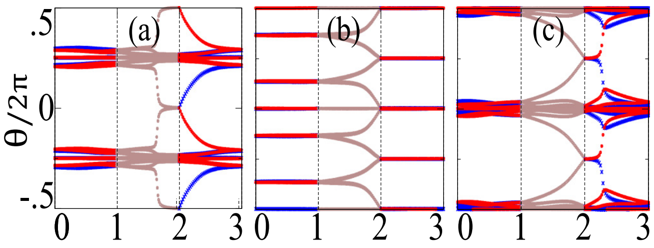

FIG. 5. *Ab initio* derived Zak phases of: (a) Ba_2Pb, (b) KHgSb, and (c) uniaxially-stressed Na_3Bi. Along the glide-invariant lines 01 and 23, we decompose the Zak phases according to their glide representations: Δ_+ is indicated by red circles and Δ_- by blue.

defined analogously with the velocities ($d\varepsilon/dt$) of surface bands instead of Zak bands. We are now ready to justify our heuristic argument for the $\mathbb{Z}_4$ classification of glide-symmetric insulators, as formulated in the introductory paragraph: Suppose our reference Fermi level lies above the Dirac node, each positive-chirality Dirac surface band [centered at $\boldsymbol{k}_{\parallel}(2) = \Gamma$] singly intersects the reference line at each of 12 and 23; each therefore contributes to χ^+ the quantity $2(0) + (-1) + 2(1)$. We may therefore interpret the deformation in Fig. 1(d) as the equivalence: $\chi^+ = 2 \equiv -2$.

III. MATERIALIZATION OF NONSYMMORPHIC TOPOLOGICAL INSULATORS

In this section, we identify three *insulating* materials which realize all three nontrivial phases in the $\mathbb{Z}_4$ classification given by $\chi^+ \equiv -\chi^-$. This classification is characterized as strong, in the sense that any nontrivial phase (with $\chi^+ \neq 0$ mod 4) cannot be realized by layering lower-dimensional glide-symmetric topological insulators [54].

As is known from topological K theory [3], the full classification of glide-symmetric surface bands is $\mathbb{Z}_4 \oplus \mathbb{Z}_2$, where the additional $\mathbb{Z}_2$ summand corresponds to a weak classification by a Kane-Mele [55] invariant (denoted $\mathcal{P}_{01} \in \{0, 1\}$) defined over the time-reversal and glide-invariant plane containing the face a. $\mathcal{P}_{01}$ may be determined by the connectivity of Zak/surface bands on the off-center glide line 01 [56]: $\mathcal{P}_{01} = 0$ corresponds to a gapped, hourglass-type connectivity along $t \in [0, 1]$ in the top row of Fig. 3 and $\mathcal{P}_{01} = 1$ to a zigzag (quantum-spin-Hall) connectivity [57,58] in the bottom row.

Having described in Fig. 3 the connectivity in each nontrivial class of $\mathbb{Z}_4 \oplus \mathbb{Z}_2$, we are ready to identify Ba_2Pb, KHgSb, and uniaxially-stressed Na_3Bi as corresponding to $(\chi^+, \mathcal{P}_{01}) = (3, 0), (2, 0), (1, 0)$, from their *ab initio*-derived Zak-band connectivity in Figs. 5(a) and 5(c). The parity of χ^+ being even (resp. odd) is in one-to-one correspondence [30] with the trivial (resp. nontrivial) phase in the time-reversal-symmetric, strong $\mathbb{Z}_2$ classification. We thus deduce that Ba_2Pb and uniaxially-stressed Na_3Bi belong to the same phase in the time-reversal-symmetric classification (as was derived by other means in previous works [36,37]) but belong to distinct $\mathbb{Z}_4$ phases in the presence of glide symmetry. This conclusion is further supported by our analysis of both compounds based on their elementary band representations [21,50,59–62]—a perspective we develop in Appendix D.

In comparison, KHgSb is trivial in the time-reversal-symmetric $\mathbb{Z}_2$ classification but nontrivial in the glide-symmetric $\mathbb{Z}_4$ classification; additional crystalline symmetries (beyond glide) in the space group (D^4_{6h}) of KHgSb are known to lead to an even finer classification [2]. It was argued in Ref. [3] that KHgSb should belong to the $\chi^+ = 2$ class based on the connectivity of its surface states; Fig. 5(b) provides evidence based on an explicit calculation of the bulk topological invariant. We remark that a recent polarized Raman scattering study [63] suggests of a low-temperature lattice instability in KHgSb; such an instability would not break glide symmetry, and we expect that $\chi^+ = 2$ should remain valid. In Appendix D, we detail the space groups and elementary band representations of these materials and further describe the stress that should be applied to Na_3Bi so that it becomes a topological insulator.

IV. PHOTOEMISSION SPECTROSCOPY OF $\mathbb{Z}_4$ INVARIANT

Let us describe how the $\mathbb{Z}_4$ invariant [cf. Eq. (2)] is measurable from PES. The velocities ($d\varepsilon/dt$) of surface states are measurable from angle-resolved PES using standard techniques [32,33]. The counting of $\mathcal{S}^{\pm}_{23}$ (resp. $\mathcal{S}^{\pm}_{01}$) further requires that we identify the glide representation ($\Delta_{\pm}$) of the pre-excited Bloch state on the glide line intersecting the surface-BZ center (resp. lying on the surface-BZ edge). We propose a spectroscopic method for identifying $\Delta_{\pm}$ on the central glide line 23 ($k_x = 0$) in the next section [Sec. V].

This method cannot be applied to determine $\Delta_{\pm}$ for the off-center glide line 01, as explained at the end of Sec. V. However, we may anyway determine the $\mathbb{Z}_4$ invariant for materials with no Fermi-level surface states along 01, in which case $\mathcal{S}^{\pm}_{01} = 0$. Indeed, there is no topological reason to expect surface states along 01 for materials with a trivial weak index ($\mathcal{P}_{01} = 0$), as explained in Sec. III. Our calculations show that all three materials (proposed in Sec. III) have $\mathcal{P}_{01} = 0$ and have no Fermi-level surface states along 01 for a perfect surface termination (i.e., ignoring surface relaxation or reconstruction). We remark that $\mathcal{P}_{01} = 0$ is guaranteed for certain space groups (including those of KHgSb and uniaxially-stressed Na_3Bi), owing to a symmetry of a discrete translation (in a direction oblique to the surface); this is elaborated on in Appendix C.

Let us address one final subtlety about the identification of $\chi^{\pm}$ (or $\mathcal{C}$) from photoemission. $\chi^{\pm}$ and $\mathcal{C}$ have been defined with respect to a fixed, Cartesian, right-handed coordinate system parametrized by (k_x, k_y, k_z). A spectroscopist who examines a solid necessarily has to pick a coordinate system and measure the topological invariants with respect to this choice. Will two measurements of $\chi^{\pm}$—of the same solid but based on different coordinates chosen by the spectroscopist—unambiguously agree?

The glide symmetry may be exploited to reduce this coordinate ambiguity: We may always choose a right-handed, Cartesian coordinate system where $\vec{\boldsymbol{x}}$ (resp. $\vec{\boldsymbol{y}}$) lies parallel to the reflection (resp. fractional translational) component of the glide, i.e., the glide maps $(x, y, z) \rightarrow (-x, y \pm R_2/2, z)$ [64]; from the experimental perspective, this presupposes some knowledge about the crystallographic orientation of a sample, as discussed further in Appendix F. This prescription does not uniquely fix the coordinate system: Supposing (x, y, z) satisfies the above condition, so would $(x', y', z') = (-x, -y, z)$, and more generally any coordinate system that is related to (x, y, z) by twofold rotations about $\vec{\boldsymbol{x}}, \vec{\boldsymbol{y}}$ or $\vec{z}$; such rotations, denoted as $p \in \{C_{2x}, C_{2y}, C_{2z}\}$, respectively, preserve the orientation (or handedness) of the coordinate system.

It follows from the above discussion that two spectroscopists, given an identical sample, may set down different coordinate systems parametrized by (x, y, z) and $(x', y', z') = p \circ (x, y, z)$, respectively; p need not be a symmetry of the solid. Following identically the instructions of this work, the two spectroscopists would determine the $\mathbb{Z}_4$ and $\mathbb{Z}$ invariants based on their chosen coordinates; suppose the first spectroscopist measures the numbers $(\chi^{\pm}, \mathcal{C})$, and the second measures $(p \circ \chi^{\pm}, p \circ \mathcal{C})$. As proven in Appendix E, for $p \in \{C_{2x}, C_{2y}\}$, $p \circ \chi^{\pm} = -\chi^{\mp}$ and $p \circ \mathcal{C} = -\mathcal{C}$. On the other hand, $C_{2z} \circ \chi^{\pm} = \chi^{\pm}$ and $C_{2z} \circ \mathcal{C} = \mathcal{C}$. In all cases, Eq. (4) is invariant. We may then draw the following conclusions depending on whether $\mathcal{C}$ is even or odd: If even (which includes the insulating case), then $\chi^{\pm} \equiv -\chi^{\mp}$ according to Eq. (4), and two right-handed (or two left-handed) spectroscopists always agree on their measured values for $\chi^{\pm}$. That is to say, $\chi^{\pm} = p \circ \chi^{\pm}$ for $p \in \{C_{2x}, C_{2y}, C_{2z}\}$. If, however, $\mathcal{C}$ is odd, two right-handed spectroscopists are only guaranteed to agree on the parity of $\chi^{\pm}$. Despite this ambiguity, once a convention for a coordinate system is fixed, the *distinction* between phases is well defined.

V. GLIDE-RESOLVED PHOTOEMISSION SPECTROSCOPY

This section is a self-contained exposition on a spectroscopic method to identify the glide representation $\Delta_{\pm}(k_y)$ of initial Bloch states (i.e., Bloch states before photoexcitation). We assume only that the reader is familiar with basic notions in the representation theory of space groups, as reviewed briefly in Sec. I.

Our method is applicable to surface or bulk photoemission. That is to say, our initial Bloch states may be localized to the surface (on which the radiation is incident) or delocalized throughout the bulk of the solid. In both cases, we focus on initial Bloch states with wave vectors on the glide-invariant line intersecting the surface-BZ center (the central glide line), as indicated by 23 in Fig. 2(a). Adopting our choice coordinates for real and quasimomentum spaces, this glide-invariant line lies at $k_x = 0$, for a glide operation g_x that maps $(x, y) \rightarrow (-x, y + R_2/2)$, with R_2 a primitive surface-lattice period.

We will first describe the basic idea in simple, intuitive terms in Sec. V A, where we specialize to normally incident, linearly polarized, and monochromatic light. We shall assume that the radiation gauge and dipole approximation are applicable to the electron-photon coupling; the dipole approximation is relaxed in the formal theory presented in Sec. V B, where we also generalize our conclusions to off-normal incident light. In the late stages of this work, the selection rule [cf. Eq. (6)] that is the main result of Sec. V A has independently been derived by Ryoo and Park [65] within the dipole approximation. Though the dipole approximation breaks down for surface photoemission induced by p-polarized light [66–68], a widely-held expectation is that the selection rule should remain valid beyond the dipole approximation; this expectation is confirmed by the pedagogical derivation in Sec. V B.

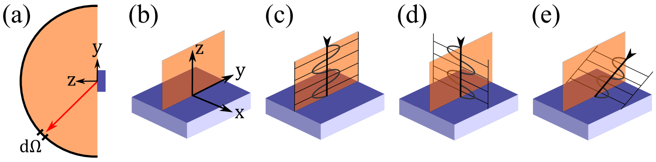

FIG. 6. (a) Cross section of the photoemission setup: A sample (colored blue) is radiated and emits photoelectrons which are collected in a hemispherical cup. (b) Our chosen coordinate system, which holds for all (a)–(e). In (a) only a constant-x cross section is drawn. (c)–(e) illustrate our favored incidence angles and polarizations. The spatial variation and directional vector of the electric field are indicated by the sinusoidal lines.

A. Basic principle

Suppose an electron—with Bloch wave function ψ_i, initial energy ε_i, and wave vector $\boldsymbol{k}_{\parallel} = (0, k_y)$—absorbs a photon and is excited to a photoelectronic state with energy ε_p. The electron-photon coupling is proportional to $\boldsymbol{a}\cdot\hat{\boldsymbol{p}}$ in the radiation gauge, where $\boldsymbol{a} \propto \vec{\epsilon}$ is the divergence-free electromagnetic vector potential, and the electromagnetic scalar potential is chosen to vanish. $\hat{\boldsymbol{p}}$ above is the electronic momentum operator, which should be distinguished from the crystal wave vector $\boldsymbol{k}$. We choose normally-incident, linearly-polarized radiation with the polarization vector $\vec{\epsilon}$ lying parallel to the glide plane; for the g_x-invariant yz plane, $\vec{\epsilon} = \vec{\boldsymbol{y}}$ is the unit vector in the y direction [cf. Fig. 6(c)]. In the dipole approximation, $\boldsymbol{a}\cdot\hat{\boldsymbol{p}}$ reduces to a spatially-homogeneous constant multiplied with $\hat{p}_y$. Since $\hat{p}_y$ is invariant under g_x and surface-parallel translations, ψ_i and the emitted photoelectron belong to the same representation of these symmetries; we shall refer to this constraint as a selection rule.

This selection rule has observable consequences for a photoelectron that is measured at the detector. This photoelectron generically has a complicated wave function with a component in vacuum that extends toward the detector and a separate component that penetrates the solid up to an escape depth [69]. Consider how a photoelectron transforms under any spacetime symmetry of a surface-terminated solid (in short, surface-preserving symmetry), as exemplified in this context by g_x and surface-parallel translations. Such transformation is completely determined by the transformation of the photoelectron's component in vacuum, because a surface-preserving isometry never maps a point inside a solid to a point outside. Since vacuum is symmetric under continuous translations and $SU(2)$ spin rotations [70], the vacuum component is simply a linear combination of plane waves with energy $\varepsilon_p \!: = (\hbar p)^2/2m$ and wave vector $\boldsymbol{p}$ (note $|\boldsymbol{p}| := p$); for each $\boldsymbol{p}$, there are two plane waves distinguished by the photoelectron spin. Due to the symmetry of discrete surface-parallel translations, the surface-parallel component of $\boldsymbol{p}$ must equal $\boldsymbol{k}_{\parallel}$—of the initial Bloch state—modulo a surface-parallel reciprocal vector $\boldsymbol{G}_{\parallel}$; each $\boldsymbol{G}_{\parallel}$ corresponds to a different angle for photoelectrons to come out of the solid, as illustrated by the fan of arrows in Fig. 1(e).

To understand the symmetry representation of the photoelectron, we must therefore analyze the symmetry properties of spin-polarized plane waves. Each g_x-invariant plane-wave state $|\phi_{\boldsymbol{p},s}\rangle$ is a tensor product $(|\phi_{\boldsymbol{p}}\rangle \otimes |s\rangle)$ of a spinless plane wave $(\langle \boldsymbol{r}|\phi_{\boldsymbol{p}}\rangle = e^{i\boldsymbol{p}\cdot\boldsymbol{r}})$ and a spinor $|s = \pm 1\rangle$ in the eigenbasis of S_x. The momentum $\boldsymbol{p}$ lies parallel to the glide plane ($p_x = 0$), and the spin orthogonal to the glide plane, such that

$$\hat{g}_x|\phi_{\boldsymbol{p},s}\rangle = -i\,s\,e^{-ip_yR_2/2}|\phi_{\boldsymbol{p},s}\rangle;\ S_x|s\rangle = s\frac{\hbar}{2}|s\rangle. \qquad (5)$$

The phase $-i\,s$ originates from reflecting $|s\rangle$ in the x direction; after all, this reflection is just the composition of spatial inversion (which acts trivially on spin) and a twofold rotation $e^{-i\pi(L_x+S_x)}$ about the x axis. The phase $e^{-ip_yR_2/2}$ in Eq. (5) originates from translating $\phi_{\boldsymbol{p}}$ by half a lattice period in the y direction. We can always express $p_y = k_y + 2\pi n/R_2$ such that k_y lies in the first Brillouin zone (BZ) and $n \in \mathbb{Z}$. Recalling from Sec. I that a Bloch state in the $\Delta_\pm(k_y)$ representation has glide eigenvalue $\pm ie^{-ik_yR_2/2}$, we conclude that $\phi_{\boldsymbol{p},s}$ transforms in the $\Delta_{-s}(k_y)$ representation if n is even and in the $\Delta_{+s}(k_y)$ representation if n is odd.

Combining this symmetry analysis with our selection rule, we find the following constraint for a photoelectron that is excited from an initial Bloch state $[\boldsymbol{k}_\parallel = (0, k_y)]$ in the $\Delta_+(k_y)$ representation. Namely, the photoelectronic plane wave $(|\phi_{\boldsymbol{p},s}\rangle)$ that is detected must also belong in the $\Delta_+(k_y)$ representation; this implies that the spin of the photoelectron is nontrivially locked to its momentum: expressing the surface-parallel component of $\boldsymbol{p}$ as $\boldsymbol{p}_\parallel = (0, p_y = k_y + 2\pi n/R_2)$, then

$$\langle S_x\rangle = s\frac{\hbar}{2} = \begin{cases} +\frac{\hbar}{2}, & \text{if} \quad n \in 2\mathbb{Z}+1 \\ -\frac{\hbar}{2}, & \text{if} \quad n \in 2\mathbb{Z} \end{cases}. \qquad (6)$$

If the initial Bloch state were in the Δ_- representation, then Eq. (6) holds with the interchange of 'odd' and 'even.' This spin-momentum locking manifests the glide symmetry of the spin-orbit interaction. As a consequence, each ray of the fan [in Fig. 1(e)], corresponding to a unique value of n, is fully spin polarized; nearest-neighbor rays always have opposing polarizations. The angle of each ray is determined by energy conservation:

$$\varepsilon_i + \hbar\omega = \frac{\hbar^2(k_y + 2\pi n/R_2)^2 + \hbar^2 p_z^2}{2m}. \qquad (7)$$

Tantalizingly, each ray may be isolated experimentally by standard spin- and angular-resolution techniques that measure $\langle S_x\rangle$ and p_y [33]; this allows us to spectroscopically identify the glide representation of an initial state.

B. One-step theory of glide-resolved photoemission

To justify this spin-momentum locking rigorously, we employ the steady-state scattering formulation [71–73] of the one-step theory [69,74,75] of photoemission. Let us consider the component H_e of the Hamiltonian that describes the solid in the absence of radiation; in the independent-electron approximation and nonrelativisitic limit [76,77], $H_e = (\hbar\hat{\boldsymbol{p}})^2/2m + V$, with V the sum of a scalar potential, the spin-orbit interaction, and in principle also the Darwin term. Since V encodes a mean-field interaction of a single electron with other electrons as well as the ionic lattice, V falls off to zero rapidly away from the solid [78]. Here, we have adopted the usual electrostatic convention for the zero of energy—as the energy of a zero-momentum plane wave in free space (far away from the solid).

Suppose ψ_i, an eigenstate of H_e with energy ε_i below the Fermi level, absorbs a single photon with energy $\hbar\omega$; i here includes all quantum numbers of the eigenstate, including the band index and the crystal wave vector. The corresponding photoelectron has energy $\varepsilon_i + \hbar\omega > 0$ and a spinor wave function of the form:

$$\Psi_{p,i} = G^+(\varepsilon_p)H_{\text{int}}\psi_i, \quad \varepsilon_i + \hbar\omega := \varepsilon_p := (\hbar p)^2/2m \qquad (8)$$

to lowest order in the electron charge [79]. Here we have introduced the advanced/retarded Green's functions: $G^\pm(\varepsilon) = (\varepsilon - H_e \pm i\delta)^{-1}$, with infinitesimal $\delta > 0$. The electron-photon coupling has the form $H_{\text{int}} = |e|(\boldsymbol{a}\cdot\hat{\boldsymbol{p}} + \hat{\boldsymbol{p}}\cdot\boldsymbol{a})/2mc$ in the temporal gauge, where the scalar potential vanishes; $\boldsymbol{a}$ here is the screened [68,75] electromagnetic vector potential in the solid. The Zeeman interaction with the spin magnetic moment typically has a small effect relative to the $\boldsymbol{a}\cdot\hat{\boldsymbol{p}}$ term [80,81] and is therefore neglected from H_{int}; a further evaluation of the Zeeman interaction is provided in Sec. VI.

Given that ψ_i belongs to a certain glide representation, we would like that the photoelectron transforms in a glide representation that is uniquely determined by the representation of ψ_i. Such a selection rule exists if the electron-photon coupling H_{int} transforms in a one-dimensional representation of glide symmetry, i.e., $\hat{g}_x H_{\text{int}}\hat{g}_x^{-1}$ equals H_{int} up to a phase, with $\hat{g}_x$ the operator that implements glide reflection [cf. Eq. (5)].

As shown in Appendix F, the desired transformation of H_{int} exists for a linearly-polarized light source, with wave vector parallel to the glide-invariant yz plane, and with the polarization vector $\vec{\epsilon}$ either orthogonal [see Figs. 6(d) and 6(e)] or parallel [Fig. 6(c)] to the glide-invariant plane. In the standard convention, we identify the orthogonal alignment as s polarization, and the parallel alignment as p polarization, though such identifications are not meaningful for normal incidence.

In the case of normal incidence, the Fresnel equations inform us that the light remains linearly polarized (with the same polarization vector $\vec{\epsilon}$) upon transmission into the solid; that is to say, the vector potential $\boldsymbol{a}$ within the solid remains parallel to $\vec{\epsilon}$. In the orthogonal alignment, $H_{\text{int}} \propto \boldsymbol{a}\cdot\hat{\boldsymbol{p}} \propto \hat{p}_x e^{-i\omega z/c}$ anticommutes with the glide operator $\hat{g}_x$; with the parallel alignment, $H_{\text{int}} \propto \hat{p}_y e^{-i\omega z/c}$ commutes [82] with $\hat{g}_x$. In the more general case of non-normal incident angles [see Fig. 6(e)], it is shown in Appendix F that

$$\hat{g}_x H_{\text{int}}\hat{g}_x^{-1} = \pm e^{-iq_yR_2/2}H_{\text{int}}, \qquad (9)$$

with the plus (resp. minus) sign applying to p (resp. s) polarization, and the additional phase factor $e^{-iq_yR_2/2}$ originating from a half-lattice translation of the photon field (having wave number q_y within the solid).

Since $\hat{g}_x$ commutes with $G^+(\varepsilon_p)$ [cf. Eq. (8)], $\Psi_{p,i}$ and $H_{\text{int}}\psi_i$ transform in the same representation of g_x. That is, if ψ_i is a Bloch function $[\boldsymbol{k}_\parallel = (0, k_y)]$ in the $\Delta_\pm(k_y)$ representation, then $\Psi_{p,i}$ belongs in the $\Delta_\mp(k_y + q_y)$ [resp.

$\Delta_\pm(k_y+q_y)$] representation for $\vec{\epsilon}$ orthogonal (resp. parallel) to the glide-invariant plane; the addition of q_y in the argument represents the absorption of the photon's momentum [cf. Eq. (9)]. Assuming the surface is clean and unreconstructed, $\Psi_{p,i}$ also transforms under discrete translations in the representation $\boldsymbol{k}_\parallel = (0, k_y+q_y)$. Let us translate these selection rules to a spin-momentum-locking constraint on the measured photocurrent. We begin with an identity relating $G^\pm$ to the free-space Green's function $G_0^\pm$:

$$G^\pm = G_0^\pm + G_0^\pm V G^\pm;\ G_0^\pm(\varepsilon) := \left(\varepsilon - \frac{(\hbar\hat{\boldsymbol{p}})^2}{2m} \pm i\delta\right)^{-1}. \quad (10)$$

The asymptotic form of $G_0^\pm$ for $|\boldsymbol{r}|:=r \gg r':=|\boldsymbol{r}'|$ is well known [83]:

$$\langle \boldsymbol{r}, s|G_0^\pm(\varepsilon_p)|\boldsymbol{r}', s'\rangle \sim -\frac{m}{\hbar^2}\frac{e^{\pm ipr}}{2\pi r}e^{\mp i\boldsymbol{p}\cdot\boldsymbol{r}'}\delta_{ss'}, \quad (11)$$

where $\vec{\boldsymbol{r}}$ is the unit vector parallel to $\boldsymbol{r}$, $\boldsymbol{p} := p\vec{\boldsymbol{r}} := (p_x, p_y, p_z)$, $|\boldsymbol{r}, s\rangle$ is an eigenstate of position and S_x operators, and $\sim$ denotes the leading asymptotic form for large r.

Let us apply the identity Eq. (10) and the asymptotic form of G_0^+ [Eq. (11)] to evaluate $\Psi_{p,i}$ defined in Eq. (8). Combining Eqs. (8)–(10), we derive

$$\Psi_{p,i}(\boldsymbol{r}, s) = \sum_{s'=\pm 1}\int d\boldsymbol{r}'\langle \boldsymbol{r}, s|G_0^+(\varepsilon_p)|\boldsymbol{r}', s'\rangle \times \langle \boldsymbol{r}', s'|(I + VG^+(\varepsilon_p))H_{\text{int}}|\psi_i\rangle. \quad (12)$$

For the scattering geometry illustrated in Fig. 6(a), we take $\boldsymbol{r}$ to be a position on the hemispherical detector and choose our spatial origin to lie within the solid. Since V vanishes rapidly away from the solid [78], the domain of integration (over $\boldsymbol{r}'$) may effectively be limited to a finite volume that is at most the order of the sample volume [84]. Assuming that the detector-to-sample distance is much greater than the sample dimension (which is valid in most modern ARPES setups), the condition $r \gg r'$ is satisfied for all $\boldsymbol{r}'$ in the domain of integration, hence we may utilize the asymptotic form of the free-space Green's function in Eq. (11). Thus, combining Eq. (12) with Eq. (11), we derive

$$\text{as } r\to\infty, \quad \Psi_{p,i}(\boldsymbol{r}, s) \sim -\frac{m}{\hbar^2}\frac{e^{ipr}}{2\pi r}\langle \Phi_{\boldsymbol{p},s}|H_{\text{int}}|\psi_i\rangle, \quad (13)$$

where $|\Phi_{\boldsymbol{p},s}\rangle$ is defined as

$$|\Phi_{\boldsymbol{p},s}\rangle := |\phi_{\boldsymbol{p},s}\rangle + G^-(\varepsilon_p)V|\phi_{\boldsymbol{p},s}\rangle. \quad (14)$$

We remind the reader that $|\phi_{\boldsymbol{p},s}\rangle$ is a plane-wave state with momentum $\boldsymbol{p}$ and spin eigenvalue $s\hbar/2$ under S_x [cf. Eq. (5)]. Equation (14) may be identified as the Lippmann-Schwinger equation [71] with the retarded Green's function; this informs us that $|\Phi_{\boldsymbol{p},s}\rangle$ is an eigenstate of H_e with the boundary condition of an inverse low-energy electron diffraction (LEED) experiment [85].

Let us evaluate the spin-resolved probability current through a solid angle element $d\Omega$ centered at $\boldsymbol{r}$, as depicted in Fig. 6(a). The current contributed by ψ_i is expressible as a Fermi golden rule:

$$\frac{dI^i_{\boldsymbol{p},s}}{d\Omega} = \frac{r^2\hbar}{m}\text{Im}[\Psi^*_{p,i}\partial_r\Psi_{p,i}]_{\boldsymbol{r},s} \sim \frac{2\pi}{\hbar}\rho_p|\langle\Phi_{\boldsymbol{p},s}|H_{\text{int}}|\psi_i\rangle|^2, \quad (15)$$

where $\rho_p := mp/(2\pi)^3\hbar^2$ is the density of plane-wave states per unit real-space volume and solid angle. The measured current at the detector is obtained by summing dI^i_s over all initial states. Equations (13) and (15) are the generalization of the inverse-LEED (or one-step) theory of photoemission (as originally formulated by Adawi [74] and Mahan [69]) to include the effect of spin. Equivalent golden-rule formulas (for spin systems) have previously been derived [81,86,87] based on a different formalism by Pendry [88].

If the initial state ψ_i were energy *non*degenerate, and the light source fully polarized, then the corresponding photocurrent would be fully spin polarized in a direction given by Eq. (13). This is because the asymptotic form of $\Psi_{p,i}$ is the product of a spherical wave and a spinor, and the latter depends only on the orientation ($\vec{\boldsymbol{r}}$) of the detector relative to the sample. (This general observation about spin polarization has been made by Park and Louie in Ref. [89]).

Going beyond this general observation, we will find that utilizing crystallographic symmetry not only uniquely determines the direction of spin polarization but also allows for a fully polarized photocurrent in the presence of energy-*degenerate* initial states. Let us therefore consider the subgroup $\mathcal{A}$ of *spatial* symmetries that are preserved in the presence of the surface, i.e., they are the (subset of) symmetries of H_e that do not involve time reversal [90]. A nonvanishing $dI^i_{\boldsymbol{p},s}$ requires that $\langle\Phi_{\boldsymbol{p},s}|H_{\text{int}}|\psi_i\rangle \neq 0$; according to the Wigner-Eckhart theorem, this further requires that

$$\Gamma^*_{\Phi_{\boldsymbol{p},s}} \otimes \Gamma_{H_{\text{int}}} \otimes \Gamma_{\psi_i} = E \oplus \ldots, \quad (16)$$

where Γ_α is the representation of α under $\mathcal{A}$, Γ^* denotes the complex-conjugate representation, and E is the trivial representation. Since spatial symmetries are represented unitarily, each element in $\mathcal{A}$ commutes with both G^- and V. Therefore, we deduce from Eq. (14) that $\Phi_{\boldsymbol{p},s}$ and $\phi_{\boldsymbol{p},s}$ belong to the same representation of A. In combination,

$$dI^i_{\boldsymbol{p},s} \neq 0 \ \Rightarrow\ \Gamma^*_{\phi_{\boldsymbol{p},s}} \otimes \Gamma_{H_{\text{int}}} \otimes \Gamma_{\psi_i} = E \oplus \ldots \quad (17)$$

summarizes a key result of this work: It states that the spin-resolved photocurrent satisfies selection rules based on the overlap of $H_{\text{int}}\psi_i$ with a spin-polarized plane wave $\phi_{\boldsymbol{p},s}$. The full generality of this result is explored in Sec. VI, but for now we content ourselves with the application at hand.

Applying Eq. (17) to the representation of discrete surface-parallel translations, we derive the well-known result that if ψ_i has crystal wave vector $\boldsymbol{k}_\parallel$ and the photon has wave vector $\boldsymbol{q}_\parallel$ within the solid, then dI^i_s is only nonvanishing for $\boldsymbol{p}_\parallel = \boldsymbol{k}_\parallel + \boldsymbol{q}_\parallel$ modulo a surface reciprocal vector. Applying Eq. (17) to the representation of glide symmetry (g_x), and to plane waves propagating parallel to the glide plane (i.e., $p_x = 0$), we derive that dI^i_s is only nonvanishing for one spin component s; which component depends on the magnitude of p_y and the glide representation of $H_{\text{int}}\psi_i$, as has been explained in Sec. V A [cf. Eq. (6)]. The result of Eq. (6) holds even for non-normal incident angles with either s or p polarization. It is worth remarking that if ψ_i were energy degenerate with a state of the *same* glide representation, the net photocurrent is obtained by summing Eq. (17) for both initial states and remains fully spin polarized according to Eq. (6). Such a twofold degeneracy of initial states is in fact enforced by time-reversal symmetry at the Brillouin-zone edge, as illustrated by the hourglass dispersion in Fig. 2(c).

For a glide-invariant initial state ψ_i with $k_x = 0$, such a full correlation between spin and momentum does *not* occur for photoelectronic plane waves that propagate in a direction nonparallel to the glide plane (i.e., $p_x = 2\pi m/a_1$ with m a nonzero integer and a_1 the primitive surface-lattice period). To explain this, consider that a one-dimensional plane wave $e^{ip_x x}$ (with $p_x \neq 0$) is a sum of two components $[\cos(p_x x) + i\sin(p_x x)]$ that transform in even and odd representations of the reflection: $x \to -x$; likewise, $\phi_{\boldsymbol{p},s}$ is the sum of two components belonging to distinct representations of g_x. Consequently, no matter the glide representation of ψ_i and no matter the magnitude of p_y, glide symmetry does not enforce $dI^i_{\boldsymbol{p},s}$ to vanish for any spin eigenvalue (s) of S_x. Restating this conclusion, the photocurrent is not expected to be spin polarized in the x direction on grounds of glide symmetry.

Finally, let us consider a glide-invariant initial state ψ_i belonging to the off-center glide line ($\bar{0}1$, $k_x = \pi/a_1$). The corresponding photoelectron must be emitted with *nonzero* wave number $p_x = q_x + \pi(2n+1)/a_1$ with $n \in \mathbb{Z}$. By the same argument (given in the previous paragraph), the photocurrent is not expected to be S_x polarized on grounds of glide symmetry. This implies that the spin-momentum-locking technique cannot be used to determine the glide representation of initial Bloch states on the off-center glide line $\bar{0}1$.

VI. DISCUSSION AND SUMMARY

We have proposed a $\mathbb{Z}_4 \oplus \mathbb{Z}$ strong classification of glide-symmetric solids (inclusive of band insulators and metals); for each nontrivial class of the $\mathbb{Z}_4$ classification, we have proposed a materialization in KHgSb, Ba_2Pb, and stressed Na_3Bi. The smoking-gun signatures of each phase are described in the photoemission of surface states. To facilitate the identification of $\chi^{\pm} \in \mathbb{Z}_4$, we have proposed a method to measure initial-state glide eigenvalues in photoemission spectroscopy. It is further shown that any two spectroscopists—employing distinct spatial coordinate systems but with the same orientation—will agree on: (a) $\chi^{\pm}$ modulo four, if $\mathcal{C}$ is even, and (b) $\chi^{\pm}$ modulo two, if $\mathcal{C}$ is odd. The implications of (a) for Ba_2Pb ($\chi^+ = -1$) and stressed Na_3Bi ($\chi^+ = +1$) is that they may be sharply distinguished through glide-resolved photoemission.

Our method to resolve glide eigenvalues exploits a spin-momentum locking that characterizes the photoemission of *any* glide-symmetric solid. In more detail, a photoelectron is emitted into vacuum as a superposition of plane waves, whose wave vectors are illustrated in Fig. 1(e) as a fan of rays; distinct rays differ by a surface reciprocal vector, and every adjacent pair of rays has opposite spin orientations.

As an orthogonal application of this locking, one may generate a photocurrent with near-perfect spin polarization by isolating one of these rays, using standard angle-resolved PES techniques. Photoemission sources of spin-polarized electrons have diverse applications as spectroscopic probes of solid-state systems [91]; such sources form the basis for spin-polarized bremsstrahlung isochromat spectroscopy [92], spin-polarized low-energy electron diffraction [93], spin-polarized electron-energy-loss spectroscopy (e.g., for the investigation of Stoner excitations [94]), and spin-polarized appearance potential spectroscopy [95]. While beam current densities of existing GaAs-based, photoemission sources are satisfactory, their spin polarization is theoretically limited to 50%, with experiments achieving just over 40% [91]; in comparison, our proposed spin polarization can in principle be complete (100%), assuming the surface-terminated solid perfectly maintains glide symmetry. It is worth remarking that a fully spin-polarized photocurrent is generally expected if the initial state is energy *non*degenerate and the light source fully polarized [89]. By utilizing crystallographic glide symmetry, our work goes beyond this general expectation in two respects: (a) the direction of spin polarization is fully determined by Eq. (6), and (b) energy-degenerate initial states (in the same glide representation) can *also* produce a fully polarized photocurrent, as discussed in Sec. V B.

For the above applications, spin-orbit-split energy bands are desirable; otherwise, distinct glide representations would be energy degenerate at each crystal wave vector [2], and their combined photoemission would result in canceling spin polarizations. Practically, the spin-orbit splitting should be larger than the energy resolution of the detector in PES. Two types of spin-orbit-split energy bands may in principle be utilized:

(i) Surface bands are generically split by spin-orbit coupling due to the absence of spatial inversion symmetry on the surface. For example, the spin-orbit splitting in the hourglass surface bands of KHgSb is predicted to be about 20 meV, [24] which is just about larger than the current energy resolution in spin-resolved PES (e.g., 7.5 meV for the ESPRESSO machine in Hiroshima Synchrotron Radiation Center [96]). It has further been predicted that compressive strain can enlarge the spin-orbit splitting of hourglass-fermion surface states [97].

(ii) Bulk bands (whose wave functions extend over the entire solid) are also spin-orbit split for certain noncentrosymmetric space groups [98]. However an additional complication may arise for spin-orbit-split bulk bands, namely that it is possible for bulk states (with different k_z and glide representations) to be *accidentally* energy degenerate; here, k_z is the wave number orthogonal to the surface. If *a priori* knowledge of the bulk band structure is unknown, then utilizing spin-orbit-split surface bands may be a safer option.

Our derivation of 100% spin polarization is based on a model of the first-order photoelectric effect with the following approximations: (i) the independent-electron approximation, (ii) a classical, Maxwell-based approximation to the electromagnetic wave in the solid, (iii) the neglect of the Zeeman interaction (with the magnetic field of the radiation) relative to the minimal coupling $\propto \boldsymbol{a} \cdot \hat{\boldsymbol{p}}$ [cf. the discussion in Sec. V B], and (iv) a surface termination which perfectly respects glide symmetry. One effect of many-body interactions in Fermi liquids is to add a continuous background to the photoemission intensity, which may reduce (but not eliminate) the full spin polarization associated to a sharp peak. (ii) is a good approximation for radiation of certain polarization and incidence angles, as explained in Sec. V B and Appendix F. (iii) is widely believed to be valid [81] and has been substantiated by model calculations [80]; however, further quantitative studies are desirable. (iv) Our prediction of 100% spin polarization also assumes that the surface of a glide-symmetric solid is also glide-symmetric. That is to say, if any surface relaxation or reconstruction occurs, we assume it preserves the glide symmetry; this assumption should be checked for any candidate material. In principle, glide-asymmetric surface defects may also reduce the spin polarization. We briefly remark on the spin polarization of the second-order photocurrent, which is induced by the absorption of two photons: For simplicity we consider normally-incident light with polarization vector parallel or orthogonal to the glide plane; in both cases, the second-order photocurrent is fully spin polarized; in the former (resp. latter) case, the second-order spin polarization is parallel (resp. antiparallel) to the first-order spin polarization [99].

A comparison with existing proposals for spin-polarized photocurrents is instructive. It is not surprising that photoemission from a spin-polarized ground state would be spin polarized [100]; such ground states exhibit either long-ranged magnetic order or spontaneously-broken spatial symmetries leading to a spin-split Fermi surface [101–105]. For ground states without spontaneous ordering, only partially spin-polarized photocurrents have been realized practically and typically only with circularly-polarized light [91]. We highlight an existing theoretical proposal which relies on neglecting the $\boldsymbol{a}\cdot\hat{\boldsymbol{p}}$ interaction in favor of the Zeeman interaction: A fully spin-polarized photocurrent may then be generated by radiating a solid (having *negligible* spin-orbit coupling) with circularly-polarized light. The neglect of the $\boldsymbol{a}\cdot\hat{\boldsymbol{p}}$ interaction is valid only for special geometric configurations [80], and even so the Zeeman-induced photocurrent is expected to be weak [81].

While we have focused on glide-symmetric solids throughout this work, we highlight a result that is generally applicable to the photoemission of any spin-orbit-coupled solid, no matter its space group. Our result is that the spin-resolved photocurrent (contributed by an initial Bloch state ψ_i) satisfies a Wigner-Eckhart-type selection rule based on the overlap of $H_{\text{int}}\psi_i$ with a spin-polarized plane-wave state, as summarized in Eq. (17). Here, our selection rules are based only on spatial symmetries that are preserved in the presence of a surface; these symmetries are determined by the exact conditions of the surface, including possible relaxation or reconstruction effects. H_{int} here is the electron-photon coupling and may in principle include either or both of the $\boldsymbol{a}\cdot\hat{\boldsymbol{p}}$ and Zeeman interactions. It should be emphasized that Eq. (17) has been derived *without* the dipole and Born approximations. In the Born approximation, the final state of photoemission [cf. Eq. (14)] is approximated as a plane wave [74]; this approximation is certainly invalid at lower photon energies [81]. Also, we remark that Eq. (17) has been derived within the one-step theory, which is more accurate [106] and more generally applicable [69,75] than the three-step theory [107,108]—only the one-step theory can describe surface photoemission.

For a final illustration, we apply Eq. (17) to solids with a reflection (or mirror) symmetry that is *not* a glide symmetry. For simplicity, we consider normally-incident light with a polarization vector lying parallel to the mirror-invariant plane. The associated photocurrent would also spread out in a fully-spin-polarized fan illustrated in Fig. 1(e), except the direction of spin polarization would *not* alternate between adjacent rays. This alternation is a fundamental property of glide symmetry, which is special for having a momentum-dependent eigenvalue $\propto e^{-ik_y/2}$. This provides a sharp distinction between the photoemission of mirror- and glide-symmetric solids. This distinction exists for both insulators and metals, in both trivial and topological categories. In particular, one may compare the surface photoemission of the mirror-symmetric topological insulator SnTe [109] with any of the glide-symmetric topological insulators that have been proposed in this work.

ACKNOWLEDGMENTS

We are grateful to Ken Shiozaki and Masatoshi Sato for informative discussions that linked this work to their K-theoretic classification. Ji Hoon Ryoo, Ilya Belospolski, Ilya Drozdov, and Peter Feibelbaum helped to clarify the discussion on photoemission spectroscopy. We especially thank Ji Hoon Ryoo, Ken Shiozaki, and Judith Höller for a critical reading of the manuscript. A.A. was supported by the Yale Postdoctoral Prize Fellowship and the Gordon and Betty Moore Foundation EPiQS Initiative through Grant No. GBMF4305 at the University of Illinois. Z.W. was supported by the CAS Pioneer Hundred Talents Program. B.A.B. acknowledges support from the Department of Energy de-sc0016239, Simons Investigator Award, the Packard Foundation, the Schmidt Fund for Innovative Research, NSF EAGER Grant No. DMR-1643312, ONR Grant No. - N00014-14-1-0330, ARO MURI Grant No. W911NF-12-1-0461, and NSF-MRSEC Grant No. DMR-1420541.

APPENDICES

The appendices are organized as follows:

(A) We briefly review symmetries in the tight-binding method and establish notation that would be used throughout the Appendix. (B) We show the equivalence between the $\mathbb{Z}_4$ invariant defined by Shiozaki-Sato-Gomi [3] and the Zak-phase expression in Eq. (1). (C) We introduce two symmetry classes of solids with glide symmetry; the two classes are distinguished by the representation of glide symmetry in the 3D Brillouin zone (BZ). In one of the two classes, the weak $\mathbb{Z}_2$ invariant is trivial, and a nonprimitive unit cell must be chosen to compute the strong $\mathbb{Z}_4$ invariant. (D) We detail the space groups and elementary band representations of Ba_2Pb, stressed Na_3Bi, and KHgSb, so as to provide a complementary perspective on their topological nontriviality. (E) We show if and how the topological invariants defined in the main text depend on the choice of coordinate system. (F) We discuss properties of the photoemission light source that allow us to utilize the selection rule (derived in Sec. V).

APPENDIX A: REVIEW OF SYMMETRIES IN THE TIGHT-BINDING METHOD

1. Review of the tight-binding method

In the tight-binding method, the Hilbert space is reduced to a finite number of atomic Löwdin orbitals $\varphi_{\boldsymbol{R},\alpha}$ for each unit cell labeled by the Bravais lattice (BL) vector $\boldsymbol{R}$ [110–112]. In Hamiltonians with discrete translational symmetry, our basis vectors are

$$\phi_{\boldsymbol{k},\alpha}(\boldsymbol{r}) = \frac{1}{\sqrt{N}} \sum_{\boldsymbol{R}} e^{i\boldsymbol{k}\cdot(\boldsymbol{R}+\boldsymbol{r}_\alpha)} \varphi_{\boldsymbol{R},\alpha}(\boldsymbol{r}-\boldsymbol{R}-\boldsymbol{r}_\alpha), \tag{A1}$$

where $\alpha = 1, \ldots, n_{\text{tot}}$, $\boldsymbol{k}$ is a crystal momentum, N is the number of unit cells, α labels the Löwdin orbital, and $\boldsymbol{r}_\alpha$ is the continuum spatial coordinate of the orbital α as measured from the origin in each unit cell. The tight-binding Hamiltonian is defined as

$$H(\boldsymbol{k})_{\alpha\beta} = \int d^d r\, \phi_{\boldsymbol{k},\alpha}(\boldsymbol{r})^* \, \hat{H} \, \phi_{\boldsymbol{k},\beta}(\boldsymbol{r}), \tag{A2}$$

where $\hat{H}$ is the single-particle Hamiltonian; $\hat{H}$ is a sum of the kinetic term, a scalar, $\boldsymbol{r}$-periodic potential (which accounts for the ionic lattice and a mean-field approximation of electron-electron interactions), as well as the spin-orbit interaction. The energy eigenstates are labeled by a band index n and defined as $\psi_{n,\boldsymbol{k}}(\boldsymbol{r}) = \sum_{\alpha=1}^{n_{\text{tot}}} u_{n,\boldsymbol{k}}(\alpha)\, \phi_{\boldsymbol{k},\alpha}(\boldsymbol{r})$, where

$$\sum_{\beta=1}^{n_{\text{tot}}} H(\boldsymbol{k})_{\alpha\beta}\, u_{n,\boldsymbol{k}}(\beta) = \varepsilon_{n,\boldsymbol{k}}\, u_{n,\boldsymbol{k}}(\alpha). \tag{A3}$$

We employ the braket notation and rewrite the above equation as

$$H(\boldsymbol{k})\, |u_{n,\boldsymbol{k}}\rangle = \varepsilon_{n,\boldsymbol{k}}\, |u_{n,\boldsymbol{k}}\rangle. \tag{A4}$$

Due to the spatial embedding of the orbitals, the basis vectors $\phi_{\boldsymbol{k},\alpha}$ are generally not periodic under $\boldsymbol{k} \to \boldsymbol{k}+\boldsymbol{G}$ for a reciprocal vector $\boldsymbol{G}$; indeed, by substituting $\boldsymbol{k}$ with $\boldsymbol{k}+\boldsymbol{G}$ in Eq. (A1), each summand acquires a phase factor $e^{i\boldsymbol{G}\cdot\boldsymbol{r}_\alpha}$ which is generally not unity. This implies that the tight-binding Hamiltonian satisfies a condition we shall refer to as 'Bloch periodic:'

$$H(\boldsymbol{k}+\boldsymbol{G}) = V(\boldsymbol{G})^{\text{-1}}\, H(\boldsymbol{k})\, V(\boldsymbol{G}), \tag{A5}$$

where $V(\boldsymbol{G})$ is a unitary matrix with elements: $[V(\boldsymbol{G})]_{\alpha\beta} = \delta_{\alpha\beta}\, e^{i\boldsymbol{G}\cdot\boldsymbol{r}_\alpha}$. Throughout this Appendix, we shall describe any matrix-valued function of $\boldsymbol{k}$ as 'Bloch periodic' if $f(\boldsymbol{k}+\boldsymbol{G}) = V(\boldsymbol{G})^{-1} f(\boldsymbol{k}) V(\boldsymbol{G})$.

In the context of insulators, we are interested in Hamiltonians with a spectral gap that is finite for all $\boldsymbol{k}$, such that we can distinguish occupied from empty bands; the former are projected by

$$\begin{aligned} P(\boldsymbol{k}) &= \sum_{n=1}^{n_{\text{occ}}} |u_{n,\boldsymbol{k}}\rangle\langle u_{n,\boldsymbol{k}}| \\ &= V(\boldsymbol{G})\, P(\boldsymbol{k}+\boldsymbol{G})\, V(\boldsymbol{G})^{\text{-1}}, \end{aligned} \tag{A6}$$

where the last equality follows directly from Eq. (A5).

2. Symmetries in glide-invariant planes

Consider a time-reversal-invariant insulator that is symmetric under the glide g_x, which is a composition of a reflection (in the x coordinate) and a translation by half a Bravais lattice vector in the y direction. We explain in this section how time-reversal and glide symmetries constrain the projection $P(\boldsymbol{k})$ to filled bands, with $\boldsymbol{k}$ lying in a glide plane; the restriction of $\boldsymbol{k}$ to the plane will be denoted $\boldsymbol{k}^r := (k_y, k_z)$.

In this section (and for the formulation of the topological invariants $\chi^\pm$), we shall concern ourselves only with glide planes wherein each wave vector is mapped to itself under glide; these glide planes are labeled *ordinary*. For example, any glide plane that includes the Brillouin-zone center is always ordinary; nonordinary glide planes only occur away from the zone center and only for certain space groups, as elaborated in Appendix C.

Let us parametrize the ordinary glide plane by $\boldsymbol{k}^r := (k_y, k_z)$, which we define to lie in the first Brillouin zone (BZ). Assuming that $\boldsymbol{G}_y = 2\pi\vec{\boldsymbol{y}}/R_2$ is a reciprocal vector, $k_y \in [-\pi, \pi]$ in units where $R_2 = 1$. $\hat{T}$ is defined as the antiunitary representation of time reversal in this plane, and $\hat{g}_x(k_y)$ as the unitary, wave-vector-dependent representation of g_x; $\hat{g}_x(k_y)$ is the product of $\exp(-ik_y/2)$ and a momentum-independent matrix U_{g_x} which commutes with $\hat{T}$, as shown in Appendix A1 of Ref. [2]. It follows that

$$\hat{T}\hat{g}_x(k_y) = \hat{g}_x(-k_y)\hat{T}, \tag{A7}$$

which we will shortly find to be useful. $P(\boldsymbol{k}^r)$, as defined in Eq. (A6), projects to a n_{occ}-dimensional vector space, with n_{occ} a multiple of four owing to glide and time-reversal symmetries, as proven in Appendix B of Ref. [2]. This vector space splits into two subspaces of equal dimension, which transform in the two representations of glide: $\Delta_\pm(k_y)$. That is, $n_{\text{occ}}/2$ number of vectors in the $\Delta_+(k_y)$ representation have the glide eigenvalue $+i\exp[-ik_y/2]$ under the operation $\hat{g}_x(k_y)$; the other $n_{\text{occ}}/2$ vectors have glide eigenvalue $-i\exp[-ik_y/2]$. The glide symmetry constrains the projection as

$$\hat{g}_x(k_y)P(\boldsymbol{k}^r)\hat{g}_x(k_y)^{-1} = P(\boldsymbol{k}^r), \tag{A8}$$

and time-reversal symmetry constrains as

$$\hat{T}P(\boldsymbol{k}^r)\hat{T}^{-1} = P(-\boldsymbol{k}^r) = V(\pm\boldsymbol{G}_y)P(\pm\boldsymbol{G}_y{-}\boldsymbol{k}^r)V(\mp\boldsymbol{G}_y), \tag{A9}$$

$$\begin{aligned} &\Rightarrow \hat{T}_\pm P(\boldsymbol{k}^r)\hat{T}_\pm^{-1} = P(\pm\boldsymbol{G}_y - \boldsymbol{k}^r),\ \text{with } \hat{T}_\pm \equiv V(\mp\boldsymbol{G}_y)\hat{T} \\ &\text{and} \quad \hat{T}_\pm^{\text{-1}} = V(\mp\boldsymbol{G}_y)\hat{T}^{\text{-1}}. \end{aligned} \tag{A10}$$

We have applied Eq. (A6) in the second equality of Eq. (A9). From Eq. (A7) and Eq. (A9), we deduce that time-reversed partner states at $\pm\boldsymbol{k}^r$ belong to orthogonal representations of $\Delta_\pm(k_y)$, as illustrated by the double-headed arrow in Fig. 2(c). Indeed,

$$\begin{aligned} &\text{if} \quad \hat{g}_x(k_y)|u_{\boldsymbol{k}^r}\rangle = \pm ie^{-ik_y/2}|u_{\boldsymbol{k}^r}\rangle, \quad \text{then} \quad \hat{g}_x(-k_y)\hat{T}|u_{\boldsymbol{k}^r}\rangle \\ &\qquad = \hat{T}\hat{g}_x(k_y)|u_{\boldsymbol{k}^r}\rangle = \mp ie^{ik_y/2}\hat{T}|u_{\boldsymbol{k}^r}\rangle. \end{aligned} \tag{A11}$$

On the other hand, time reversal imposes a different constraint on the glide representations at the $k_y = \pm\pi$ edges of the glide plane: $\hat{T}_\pm$ maps $\boldsymbol{k}^r = (\pm\pi, k_z) \to (\pm\pi, -k_z)$, and $\hat{T}_\pm$-related states belong to the same glide representation, as illustrated by curved arrows in Fig. 2(c) and double-headed arrows in Fig. 2(d). This result follows from

$$\begin{aligned} \hat{g}_x(\pm\pi)\hat{T}_\pm &= \hat{g}_x(\pm\pi)V(\mp\boldsymbol{G}_y)\hat{T} \\ &= e^{-i\boldsymbol{G}_y\cdot\vec{\boldsymbol{y}}/2}V(\mp\boldsymbol{G}_y)\hat{g}_x(\pm\pi)\hat{T} \\ &= e^{-i\pi}V(\mp\boldsymbol{G}_y)\hat{T}\hat{g}_x(\mp\pi) = \hat{T}_\pm\hat{g}_x(\pm\pi), \end{aligned} \tag{A12}$$

and the reality of the eigenvalues of $\hat{g}_x(\pm\pi)$. The second equality in Eq. (A12) follows from Eq. (A24) in Ref. [2].

To restate the above result in slightly different words, within an ordinary glide plane, any time-reversed partner states which lie at k_y and $-k_y$ belong in opposite glide representations; this statement applies to $k_y = 0$. In comparison, time-reversed states with equal wave number ($k_y = \pi$) belong in the same glide representation; note at $k_y = \pi$ that the glide eigenvalue is real. This will be helpful in formulating the $\mathbb{Z}_4$ invariant in Appendix B.

APPENDIX B: ZAK-PHASE EXPRESSION OF STRONG $\mathbb{Z}_4$ INVARIANT

We show the equivalence between the $\mathbb{Z}_4$ invariant defined by Shiozaki *et al.* [3] and the Zak-phase expression Eq. (1). Consider the bent quasimomentum region (abc) drawn in Fig. 3(a), which is the union of three faces a (red), b (green), and c (orange): a and c are each half of a glide plane, and b is a half-plane orthogonal to both a and c; due to the periodicity of the Brillouin torus, abc has the topology of an open cylinder and is parametrized by orthogonal coordinates $\boldsymbol{k} = (t, k_z)$, with $t \in [0, 3]$ and $k_z \in [0, 2\pi)$; $k_z = 0$ is identified with $k_z = 2\pi$. We define $\mathcal{L}(t)$ as constant-t circles in abc, as illustrated by oriented dashed lines in Fig. 2(b); the sign of $\pm\mathcal{L}(t)$ indicates its orientation, and abc is bounded by $\mathcal{L}(0) - \mathcal{L}(3)$.

In the half-plane b [$t \in [1, 2]$, corresponding to k_x varying in the interval $(-\pi, 0)$], we define the connection and curvature as

$$\text{for } \boldsymbol{k} = (t, k_z) \in b, \quad \mathrm{Tr}[\boldsymbol{A}(\boldsymbol{k})] = \sum_{i=1}^{n_{\mathrm{occ}}} \langle u_{i,\boldsymbol{k}} | \nabla_{\boldsymbol{k}} u_{i,\boldsymbol{k}} \rangle,$$
$$F(\boldsymbol{k}) \equiv \partial_t \mathrm{Tr}[\boldsymbol{A}_z(\boldsymbol{k})] - \partial_z \mathrm{Tr}[\boldsymbol{A}_t(\boldsymbol{k})]. \tag{B1}$$

Here, $\boldsymbol{A} = (A_t, A_z)$ with $A_t = \sum_i \langle u_{i,\boldsymbol{k}} | \partial_t u_{i,\boldsymbol{k}} \rangle$ and $A_z = \sum_i \langle u_{i,\boldsymbol{k}} | \partial_{k_z} u_{i,\boldsymbol{k}} \rangle$. Choosing wave functions in a and c to be eigenstates of the glide operation, they divide into two equally-numbered sets according to their glide eigenvalues, which fall into either branch of $\Delta_\eta(k_y) = \eta\, i \exp(-ik_y/2)$, with $\eta = \pm 1$. We distinguish between these two sets by modifying our wave-function labels to $\{u^\eta_{n,\boldsymbol{k}} | n = 1, \ldots, n_{\mathrm{occ}}/2\}$. We then define the glide-projected, Berry connection, and its corresponding curvature as

$$\text{for } \boldsymbol{k} \in a \cup c, \quad \mathrm{Tr}[\boldsymbol{A}^\eta(\boldsymbol{k})] = \sum_{i=1}^{n_{\mathrm{occ}}/2} \langle u^\eta_{i,\boldsymbol{k}} | \nabla_{\boldsymbol{k}} u^\eta_{i,\boldsymbol{k}} \rangle,$$
$$F^\eta(\boldsymbol{k}) \equiv \partial_t \mathrm{Tr}\big[A^\eta_z(\boldsymbol{k})\big] - \partial_z \mathrm{Tr}\big[A^\eta_t(\boldsymbol{k})\big]. \tag{B2}$$

Shiozaki *et al.* defined a $\mathbb{Z}_4$ invariant by

$$\chi^\eta = 2\mathcal{P}^\eta(0) - 2\mathcal{P}^\eta(3) + \frac{i}{2\pi}\bigg[2\int_a F^\eta d^2\boldsymbol{k}$$
$$+2\int_c F^\eta d^2\boldsymbol{k} + \int_b F\, d^2\boldsymbol{k}\bigg], \tag{B3}$$

with the polarization (in the Δ_η representation) defined as

$$\mathcal{P}^\eta(t) \equiv \frac{i}{2\pi} \int_{\mathcal{L}(t)} \mathrm{Tr}[\boldsymbol{A}^\eta(\boldsymbol{k})] \cdot d\boldsymbol{k}. \tag{B4}$$

Included in Shiozaki's definition is a gauge constraint for the wave functions on the boundary $[\mathcal{L}(0) - \mathcal{L}(3)]$.

Before defining this constraint in complete generality, let us develop some intuition by considering a specific realization. For noncentrosymmetric space groups, energy bands in each glide subspace are twofold connected along $\mathcal{L}(3)$ [also true for $\mathcal{L}(0)$], due to the Kramers-degenerate points at $k_z = 0$ and π, as illustrated in Fig. 2(d); note here that the glide eigenvalue is real, hence time-reversal related states belong to the same glide representation. For each pair of energy bands (within one glide subspace), one energy band may be denoted $u^\eta_{\alpha,\boldsymbol{k}}$ and the other $u^\eta_{\bar{\alpha},\boldsymbol{k}}$, as illustrated in Fig. 2(d). As is well known, any energy eigenfunction of a Hamiltonian is only well defined up to a phase (which here can depend on $\boldsymbol{k}$). Here, it is possible to choose this phase (or gauge) such that

$$\text{for } t \in \{0, 3\}, \quad \big|u^\eta_{\alpha,t,-k_z}\big\rangle = T_t \big|u^\eta_{\bar{\alpha},t,k_z}\big\rangle,$$
$$\big|u^\eta_{\bar{\alpha},t,-k_z}\big\rangle = -T_t \big|u^\eta_{\alpha,t,k_z}\big\rangle, \tag{B5}$$

with T_0 [T_3] the antiunitary representation of time reversal at the time-reversal invariant line $\mathcal{L}(0)$ [$\mathcal{L}(3)$]. We have shown in Appendix A 2 that time-reversed partner states at $k_y = \pi$ belong in the same glide representation (here the glide eigenvalues is real); we may directly identify $T_3 = \hat{T}_+$ in Eq. (A10). By imposing Eq. (B5) on the wave function, the invariant defined by Shiozaki becomes well-defined modulo four [3]. More generally, Eq. (B3) is well defined with the following gauge constraint: decompose each glide subspace (within the filled-band subspace) into $n_{\mathrm{occ}}/4$ pairs of bands [labelled by $\{u^\eta_{\alpha,\boldsymbol{k}}, u^\eta_{\bar{\alpha},\boldsymbol{k}} | \boldsymbol{k} \in \mathcal{L}(0) - \mathcal{L}(3),\ \alpha = 1, \ldots, n_{\mathrm{occ}}/4\}$], such that each of $u^\eta_{\alpha,\boldsymbol{k}}$ and $u^\eta_{\bar{\alpha},\boldsymbol{k}}$ is first-order differentiable in k_z and together satisfy Eq. (B5).

Calculating the $\mathbb{Z}_4$ invariant through Eq. (B3) requires that we find glide-projected wave functions that are both first-order differentiable along the boundary of abc [$\mathcal{L}(0)-\mathcal{L}(3)$] and constrained as in Eq. (B5). In the rest of this section, we reformulate Eq. (B3) as an index [Eq. (1)] that is extractable from the Wilson loop of the Berry gauge field, whose basic properties we review in Appendix B 1. One advantage of a Zak-phase calculation is that it may be done without fixing a gauge; in comparison, the necessity of imposing a differentiable gauge [satisfying Eq. (B5)] makes Eq. (B3) difficult to compute in practice. Our reformulation is a generalization of Refs. [47,113] for insulators with glide symmetry. To organize this Appendix section, we divide χ^η into two additive contributions: χ^η_{ac} from the glide-invariant faces a and c, and χ_b from the glide-variant face b.

$$\chi^\eta = \chi_b + \chi^\eta_{ac}$$
$$\chi_b = \frac{i}{2\pi} \int_b F\, d^2\boldsymbol{k} \tag{B6}$$
$$\chi^\eta_{ac} = 2[\,\mathcal{P}^\eta(0) - \mathcal{P}^\eta(3)\,] + \frac{i}{\pi}\bigg[\int_a F^\eta d^2\boldsymbol{k} + \int_c F^\eta d^2\boldsymbol{k}\bigg]. \tag{B7}$$

We tackle χ_b in Appendix B 1 e, and χ^η_{ac} in Appendix B 2.

1. Review of Wilson loops

a. Basic definition

We consider the parallel transport of occupied Bloch waves around a momentum loop $\mathcal{L}$, where at each $\boldsymbol{k} \in \mathcal{L}$ a spectral gap separates a set of lower-energy, occupied states (numbering $n_{\rm occ}$) from a higher-energy, unoccupied subspace. The $n_{\rm occ}$-by-$n_{\rm occ}$ matrix representing such parallel transport is known as the Wilson loop [49], and it may be expressed as the path-ordered exponential (denoted by $\overline{\exp}$) of the Berry-Wilczek-Zee non-Abelian connection [49,114]:

$$\mathcal{W}[\mathcal{L}] \equiv \overline{\exp}\left[-\int_{\mathcal{L}} d\boldsymbol{k}\cdot\boldsymbol{A}(\boldsymbol{k})\right], \quad \boldsymbol{A}_{ij}(\boldsymbol{k}) = \langle u_{i,\boldsymbol{k}}|\nabla_{\boldsymbol{k}} u_{j,\boldsymbol{k}}\rangle,$$
$$i, j = 1, \dots, n_{\rm occ}, \tag{B8}$$

where $|u_{j,\boldsymbol{k}}\rangle$ belongs to the filled-band subspace of the tight-binding Hamiltonian in Eq. (A4); in keeping with the generality of this review, we will not adopt the specific gauge choice in Eq. (B5). Henceforth, we consider only noncontractible loops within the 2D subregion *abc* [cf. Fig. 2(a)] parametrized by $t \in [0, 3]$ and $k_z \in [-\pi, \pi]$; each loop is oriented parallel to $\vec{z}$ and lies at fixed t, as illustrated by the triple-headed arrow in Fig. 2(a); we streamline our notation from $\mathcal{W}[\mathcal{L}(t)]$ to

$$\mathcal{W}(t) \equiv \overline{\exp}\left[-\int_{\mathcal{L}(t)} dk_z\, A_z(t, k_z)\right]. \tag{B9}$$

To calculate $\mathcal{W}(t)$ from this expression, it is implicit from the definition of A_z that a first-order differentiable basis for $u_{i,\boldsymbol{k}}$ is needed. Moreover, to uniquely define the eigenspectrum of $\mathcal{W}(t)$, we insist that this basis further satisfies the condition [48]:

$$\forall\ i \in \{1, \dots, n_{\rm occ}\}, \qquad \left|u_{i,\boldsymbol{k}+\boldsymbol{G}_z}\right\rangle = V(-\boldsymbol{G}_z)|u_{i,\boldsymbol{k}}\rangle. \tag{B10}$$

That such a basis can be found follows from the Bloch periodicity of the Bloch Hamiltonian in Eq. (A5), and so we shall refer to Eq. (B10) as the Bloch-periodic gauge.

b. The gauge-independent Wilson loop

It is advantageous to equivalently formulate the $\mathcal{W}$ eigenvalues as the unimodular eigenvalues of a related operator that is gauge independent. Following our treatment in Ref. [48] with slightly different notation, we define an operator that effects parallel transport in the Löwdin-orbital basis as

$$\hat{W}_{k_2,k_1}(t) = \prod_{k_z}^{k_2\leftarrow k_1} P(t, k_z). \tag{B11}$$

Here, we uniquely specify the path from $(t, k_1) \to (t, k_2)$ by choosing $k_z \in [k_2, k_1]$ to always lie in $[-\pi, \pi]$; the right-hand side of Eq. (B11) indicates a path-ordered product of projections [defined in Eq. (A6)] where k_z assumes any discrete value $2\pi m/N_z$ between k_1 and k_2, for integral m. $\hat{W}_{k_2,k_1}(t)$ defines a map from $\mathcal{B}(t, k_1)$ to $\mathcal{B}(t, k_2)$, where $\mathcal{B}(\boldsymbol{k})$ is the $n_{\rm occ}$-dimensional vector space spanned by the filled bands $(\{u_{j,\boldsymbol{k}}\})$ at $\boldsymbol{k}$. The Bloch periodicity of the Bloch Hamiltonian [Eq. (A5)] implies that $V(\boldsymbol{G}_z)$ (with $\boldsymbol{G}_z \equiv 2\pi\vec{z}$) is a map from $\mathcal{B}(t, k_z)$ to $\mathcal{B}(t, k_z{-}2\pi)$, and therefore the composition of $V(\boldsymbol{G}_z)$ and $\hat{W}$ (defined with a curly $\hat{\mathcal{W}}$, which is to be distinguished from $\hat{W}$) is a map:

$$\hat{\mathcal{W}}(t) \equiv V(\boldsymbol{G}_z)\hat{W}_{\pi,-\pi}(t) :\ \mathcal{B}(t, -\pi) \to \mathcal{B}(t, -\pi). \tag{B12}$$

In the limit $N_z \to \infty$, k_z becomes a continuous variable, and we may identify $\mathcal{W}$ in Eq. (B8) as a matrix representation of curly $\hat{\mathcal{W}}$ in a basis of $\mathcal{B}(t, -\pi)$ (the filled-band subspace at the base point of the loop) [48]:

$$[\mathcal{W}(t)]_{ij} = \langle u_{i,(t,-\pi)}|\, \hat{\mathcal{W}}(t)\, |u_{j,(t,-\pi)}\rangle. \tag{B13}$$

Here, $i = 1, \dots, n_{\rm occ}$ labels the basis vector and need not label an energy band. We therefore refer to curly $\hat{\mathcal{W}}$ as the gauge-independent Wilson loop. The full eigenspectrum of $\mathcal{W}$ comprises the unimodular eigenvalues of $\hat{\mathcal{W}}$, which we label by $\exp[i\theta_{n,t}]$ with $n = 1, \dots, n_{\rm occ}$. The form of $\mathcal{W}$ in Eq. (B13) manifests the gauge invariance of its eigenspectrum, since if

$$|u_{j,(t,-\pi)}\rangle \to \sum_{i=1}^{n_{\rm occ}} |u_{i,(t,-\pi)}\rangle S_{ij}, \ \text{ with } S \in U(n_{\rm occ}),$$
$$\text{then } \ \mathcal{W} \to S^{\dagger}\mathcal{W}S. \tag{B14}$$

We remark that the $\mathcal{W}$ eigenvalues are also independent of the base point of the loop [48]; our choice of $(t, -\pi)$ as the base point merely renders certain symmetries transparent, as will be made evident in Appendix B 2.

c. Relation of the Wilson loop to polarization

It is useful to relate the Wilson loop to the polarization [115], defined as the line integral of the $U(1)$ Berry connection:

$$\mathcal{P}(t) := \frac{i}{2\pi}\int_{\mathcal{L}(t)} {\rm Tr}[\boldsymbol{A}(\boldsymbol{k})]\cdot d\boldsymbol{k}. \tag{B15}$$

We caution that $\mathcal{P}$ is the expectation value of a discrete position operator (taking only discrete values corresponding to the centers of localized, tight-binding basis vectors) [35,48], rather than that of the usual continuum position operator [115]. Implicit in the definition of the Wilson loop [Eq. (B8)] is that wave functions are first-order differentiable in k_z and Bloch periodic in $\boldsymbol{G}_z$—this would also imply that the polarization quantity in Eq. (B15) is well defined. The polarization is related [48] to the $U(n_{\rm occ})$ Wilson loop through:

$$\mathcal{P}(t) \equiv -\frac{i}{2\pi}\ln\det[\,\mathcal{W}(t)\,]. \tag{B16}$$

Throughout this section, $\equiv$ denotes an equivalence up to addition or subtraction of an integer. As with all polarization quantities, this integer ambiguity [115] reflects the discrete translational symmetry in $\vec{z}$. Defining $\{\exp[i\theta_j(t)]|\}_{j=1}^{n_{\rm occ}}$ as the eigenvalues of $\mathcal{W}(t)$, Eq. (B16) is expressible as

$$\mathcal{P}(t) \equiv \frac{1}{2\pi}\sum_{j=1}^{n_{\rm occ}} \theta_j(t). \tag{B17}$$

To prove the equivalence of $\mathbb{Z}_4$ invariants, it is useful (as an intermediate step) to work in a special basis (denoted $\{\tilde{u}_{j,\boldsymbol{k}}\}_{j=1}^{n_{\rm occ}}$) of the filled-band subspace spanned by $\{u_{j,\boldsymbol{k}}\}_{j=1}^{n_{\rm occ}}$. The new basis is defined to satisfy two (related) properties: (i) for each j,

$$\tilde{\mathcal{P}}_j(t) := \frac{i}{2\pi}\int_{\mathcal{L}(t)} \langle \tilde{u}_{j,\boldsymbol{k}}|\nabla_{\boldsymbol{k}}\tilde{u}_{j,\boldsymbol{k}}\rangle\cdot d\boldsymbol{k} \equiv \frac{\theta_j(t)}{2\pi}. \tag{B18}$$

(ii) The Fourier transform of $\tilde{\psi}_{j,\boldsymbol{k}}(\alpha) := e^{i\boldsymbol{k}\cdot(\boldsymbol{R}+\boldsymbol{r}_\alpha)}\tilde{u}_{j,\boldsymbol{k}}$ with respect to k_z is a hybrid Wannier function [48,116] that is an eigenstate of the z position operator projected to the filled-band subspace; such eigenstates are always maximally localized [117] in the z direction. We refer to $\{\tilde{u}_{j,\boldsymbol{k}}\}_{j=1}^{n_{\text{occ}}}$ as the *maximally-localized basis/gauge*. Due to their nice localization properties in real space, the maximally-localized basis has found applications in several contexts [48,118,119]; we briefly review how this basis is constructed.

d. Review

To construct this special basis, we first diagonalize the gauge-independent Wilson loop [Eq. (B12)] at the base point ($k_z = -\pi$) as

$$\hat{\mathcal{W}}(t)|\tilde{u}_{n,(t,-\pi)}\rangle = e^{i\theta_{n,t}}|\tilde{u}_{n,(t,-\pi)}\rangle. \tag{B19}$$

We remind the reader that $\hat{W}$ is an $n_{\text{tot}} \times n_{\text{tot}}$ matrix operator with only n_{occ} unimodular eigenvalues (the rest being zero). Basis vectors away from the base point are then constructed by parallel transport, composed with a multiplicative phase factor [35,48,113]:

$$\left|\tilde{u}_{n,(t,k_z)}\right\rangle = e^{-i(k_z+\pi)\theta_n/2\pi}\hat{W}_{k_z,-\pi}(t)|\tilde{u}_{n,(t,-\pi)}\rangle. \tag{B20}$$

Note that $\tilde{u}_{n,(t,k_z)}$ diagonalizes the gauge-independent Wilson loop with base point k_z. Owing in part to the phase factor in Eq. (B20), $\tilde{u}_{n,(t,k_z)}$ satisfies the Bloch-periodicity condition:

$$\begin{aligned}|\tilde{u}_{n,(t,\pi)}\rangle &= e^{-i\theta_n}V(-\boldsymbol{G}_z)V(\boldsymbol{G}_z)\hat{W}_{\pi,-\pi}(t)|\tilde{u}_{n,(t,-\pi)}\rangle\\ &= e^{-i\theta_n}V(-\boldsymbol{G}_z)\hat{\mathcal{W}}(t)|\tilde{u}_{n,(t,-\pi)}\rangle = V(-\boldsymbol{G}_z)|\tilde{u}_{n,(t,-\pi)}\rangle;\end{aligned} \tag{B21}$$

in the last equality, we utilized that $\tilde{u}$ is an eigenstate of the gauge-independent Wilson loop [cf. Eq. (B19)]. We remark that the Berry connection evaluated with $\tilde{u}_{n,(t,k_z)}$ equals

$$\left\langle \tilde{u}_{m,(t,k_z)} \middle| \frac{\partial \tilde{u}_{n,(t,k_z)}}{\partial k_z} \right\rangle = -i\delta_{mn}\frac{\theta_m}{2\pi}, \tag{B22}$$

which generically does not vanish. It is instructive to demonstrate that these basis functions are orthonormal away from the base point, assuming such is true for the base point. Dropping the constant label t in this demonstration,

$$\begin{aligned}\langle \tilde{u}_{m,k_z}|\tilde{u}_{n,k_z}\rangle &= \langle \tilde{u}_{m,-\pi}|\hat{W}_{-\pi,k_z}\hat{W}_{k_z,-\pi}|\tilde{u}_{n,-\pi}\rangle\\ &= \langle \tilde{u}_{m,-\pi}|\tilde{u}_{n,-\pi}\rangle = \delta_{m,n}.\end{aligned} \tag{B23}$$

In the second equality, we applied that parallel transport within the valence bands is unitary, and therefore $\hat{W}_{-\pi,k_z}\hat{W}_{k_z,-\pi}$ acts on any state in $\mathcal{B}(-\pi)$ as the identity operator.

e. Relation of the Wilson loop to the integral of the curvature

Let us consider the area integral of the Berry curvature over faces a, b, or c; any of these faces is parametrized by $k_z \in [0, 2\pi)$ and $t \in [t_1, t_2]$ with $t_2 > t_1$. We can always choose the wave function (in a face) to be smooth with respect to t and k_z [62]. We may then utilize Stoke's theorem to convert the area integral to a line integral of the Berry connection over the face's boundary; in the Bloch-periodic gauge of Eq. (B10), the line integral over the line segments orthogonal to $\vec{z}$ cancel, and what remains is:

$$\frac{i}{2\pi}\int F(\boldsymbol{k})d^2k = \mathcal{P}(t_2) - \mathcal{P}(t_1). \tag{B24}$$

We will find it useful to evaluate the area integral with the maximally-localized basis defined in Eqs. (B19), (B20), and (B21); then applying Eq. (B17) to Eq. (B25), we obtain

$$\frac{i}{2\pi}\int F(\boldsymbol{k})d^2k = \frac{1}{2\pi}\sum_{j=1}^{n_{\text{occ}}}[\theta_j(t_2) - \theta_j(t_1)]. \tag{B25}$$

By our assumption that basis vectors are smooth in t, we must choose a branch for $\theta_j(t)$ that is differentiable in t for $t \in [t_1, t_2]$, and therefore,

$$\int F(\boldsymbol{k})d^2k = i\sum_{j=1}^{n_{\text{occ}}}\int_{t_2}^{t_1}\frac{d\theta_j}{dt}dt := i\sum_{j=1}^{n_{\text{occ}}}\int_{t_2}^{t_1}d\theta_j. \tag{B26}$$

An immediate implication is that

$$\chi_b = \frac{i}{2\pi}\int_b F(\boldsymbol{k})d^2k = \frac{1}{2\pi}\sum_{j=1}^{n_{\text{occ}}}\int_1^2 d\theta_j. \tag{B27}$$

2. Expressing χ^{η}_{ac} with the Wilson loop

In this subsection, we restrict our discussion to the glide-invariant half-planes a and c, as illustrated in Figs. 3(a) and 3(b). The component of χ^{η} [recall Eq. (B3)] contributed by a and c has been defined as χ^{η}_{ac} in Eq. (B7). It is known from Ref. [3] that χ^{η}_{ac} is well-defined modulo 4, if we insist, at $\bar{t} \in \{0, 3\}$, that the wave functions satisfy the time-reversal constraint in Eq. (B5).

The goal of this section is to express χ^{η}_{ac} [as defined in Eq. (B7)] equivalently as

$$\chi^{\eta}_{ac} = \frac{1}{\pi}\sum_{j=1}^{n_{\text{occ}}/2}\left[\theta^{\eta}_j(0) - \theta^{\eta}_j(3) + \int_0^1 d\theta^{\eta}_j + \int_2^3 d\theta^{\eta}_j\right], \tag{B28}$$

where $\theta^{\eta}_j(t)$ is the phase of the jth eigenvalue of the Wilson loop $[\mathcal{W}^{\eta}(t)]$ projected to the Δ_{η} glide representation. To clarify, if we begin at the base point of $\mathcal{L}(t)$ ($t \in [0, 1]$ or [2,3]) with a Bloch state in the $\Delta_{\eta}(k_y)$ representation, such a Bloch state remains in the $\Delta_{\eta}(k_y)$ representation as it is parallel transported in the z direction [50]. Consequently, the $n_{\text{occ}}\times n_{\text{occ}}$ Wilson loop diagonalizes into two $(n_{\text{occ}}/2)\times(n_{\text{occ}}/2)$ blocks, which we define as $\mathcal{W}^{\eta}(t)$; the superscript $\eta \in \pm$ distinguishes between the two glide representations. For Eq. (B28) to be a well-defined modulo four, we impose that θ^{η}_j is first-order differentiable with respect to t and that $\theta^{\pm}_j(t)$ are *pairwise degenerate* at $t = 0$ and 3. To clarify 'pairwise degeneracy,' we mean that for any Zak band with phase $\theta^{+}_j(0)$, we pick a branch for a distinct Zak band (labelled j') such that $\theta^{+}_{j'}(0) = \theta^{+}_j(0)$ (viewed as a strict equality, not an equivalence modulo 2π), so that $\sum_{j=1}^{n_{\text{occ}}/2}\theta^{+}_j(0)$ is uniquely defined modulo 4π.

To prove the equivalence of Eq. (B7) with Eq. (B28), we adopt the following strategy. Beginning with the filled-band subspace in each glide representation, we pick a basis that is maximally localized in the z direction [cf. Eqs. (B19)–(B21)] and simultaneously satisfies the time-reversal-symmetric gauge constraint [Eq. (B5)]. If such a basis (denoted $\tilde{u}^{\eta}_{\alpha,\boldsymbol{k}}, \tilde{u}^{\eta}_{\bar{\alpha},\boldsymbol{k}}$) can be found, then we may evaluate all terms in Eq. (B28) and Eq. (B7) in this special basis and see straightforwardly that they are identical. By 'evaluating... in this special basis,' we mean that we can express all Zak phases in Eq. (B28) as

$$\theta^\eta_\alpha = i\int_{\mathcal{L}} \langle \tilde{u}^\eta_{\alpha,\boldsymbol{k}} | \nabla_{\boldsymbol{k}} \tilde{u}^\eta_{\alpha,\boldsymbol{k}}\rangle \cdot d\boldsymbol{k} \tag{B29}$$

(and an identical expression with $\alpha \to \bar{\alpha}$); we can express the quantities occurring in Eq. (B7) as

$$\begin{aligned} \mathcal{P}^\eta(t) &= \frac{1}{2\pi}\left(\sum_{\alpha=1}^{n_{\text{occ}}/2} \theta^\eta_\alpha(t) + \sum_{\bar{\alpha}=1}^{n_{\text{occ}}/2} \theta^\eta_{\bar{\alpha}}(t)\right), \qquad t = 0, 3 \\ \frac{i}{2\pi}\int_a F^\eta(\boldsymbol{k}) d^2k &= \frac{1}{2\pi}\left(\sum_{\alpha=1}^{n_{\text{occ}}/2} \int_0^1 d\theta^\eta_\alpha + \sum_{\bar{\alpha}=1}^{n_{\text{occ}}/2} \int_0^1 d\theta^\eta_{\bar{\alpha}}\right), \end{aligned} \tag{B30}$$

(and an identical expression with $a \to c$ and $\int_0^1 \to \int_2^3$). Equation (B30) follows from our previously-derived Eq. (B17) and Eq. (B26).

Let us now prove that, indeed, such a basis can be found. While we have demonstrated how to construct the maximally-localized basis in Eqs. (B19)–(B21), we have not shown that the time-reversal constraint can be simultaneously and consistently imposed. Specifically, we would show that our maximally-localized basis vectors $\{\tilde{u}^\eta_{j,\boldsymbol{k}}\}_{j=1}^{n_{\text{occ}}/2}$ can be relabelled as pairs of $\{\tilde{u}^\eta_{\alpha,\boldsymbol{k}}, \tilde{u}^\eta_{\bar{\alpha},\boldsymbol{k}}\}_{\alpha=1}^{n_{\text{occ}}/4}$, such that each pair $(\alpha, \bar{\alpha})$ satisfies Eq. (B5) with $u \to \tilde{u}$.

Proof: Let us focus on the glide- and time-reversal-invariant lines $\mathcal{L}(0)$ and $\mathcal{L}(3)$. The proof is essentially identical for either line, so let us just focus on $\mathcal{L}(3)$. We begin by defining $\tilde{u}^\eta_{n,(t=3,k_z)}$ as a basis vector in $\mathcal{B}^\eta(3, k_z)$ (the filled-band subspace in the η glide representation) satisfying three maximally-localized conditions Eqs. (B19)–(B21). Our proof is eased by equivalently expressing two of these three conditions [Eq. (B19) and (B20)] as

$$\begin{aligned} V(\boldsymbol{G}_z)\hat{W}_{2\pi,0}(3)\big|\tilde{u}^\eta_{n,(3,0)}\big\rangle &= e^{i\theta^\eta_{n,3}}\big|\tilde{u}^\eta_{n,(3,0)}\big\rangle, \\ \big|\tilde{u}^\eta_{n,(3,k_z)}\big\rangle &= e^{-ik_z\theta^\eta_n/2\pi}\hat{W}_{k_z,0}(3)\big|\tilde{u}^\eta_{n,(3,0)}\big\rangle. \end{aligned} \tag{B31}$$

In the above equations, we have, for analytic convenience, shifted the base point of the loop from $k_z = -\pi$ to $k_z = 0$, and $\hat{W}_{k_2,k_1}$ has been defined in Eq. (B11); note that $\{e^{i\theta^\eta_n}\}$ is invariant under changes of the base point [48]. $\tilde{u}^\eta_{n,(3,k_z)}$ occurring in the second line of Eq. (B31) is an eigenstate of the gauge-independent Wilson loop with base point $k_z = 0$. The first line of Eq. (B31) leads equivalently to the inverse-eigenvalue equation:

$$\hat{W}_{0,2\pi}(3)V(-\boldsymbol{G}_z)\big|\tilde{u}^\eta_{n,(3,0)}\big\rangle = e^{-i\theta^\eta_{n,3}}\big|\tilde{u}^\eta_{n,(3,0)}\big\rangle, \tag{B32}$$

which follows from $\hat{W}_{0,2\pi}(3)V(-\boldsymbol{G}_z)V(\boldsymbol{G}_z)\hat{W}_{2\pi,0}(3)$ acting as the identity map in $\mathcal{B}(3, 0)$, the filled-band subspace.

Following our discussion in Appendix A 2, we would generate a basis vector in $\mathcal{B}^\eta(3, -k_z)$ by time reversing $\tilde{u}^\eta_{\alpha,(3,k_z)}$. The operator representation of time reversal in $\mathcal{L}(3)$ (where $k_y = \pi$) is $\hat{T}_+$, as defined in Eq. (A10); we remind the reader that any $\hat{T}_+$-related pair of Bloch states (at $k_y = \pi$) belong in the *same* glide representation Δ_η. From Eq. (B11) and Eq. (A10), we deduce the effect of time reversing the Wilson-line operators:

$$\hat{T}_+\hat{W}_{k_2,k_1}(3)\hat{T}_+^{-1} = \hat{W}_{-k_2,-k_1}(3), \tag{B33}$$

and also the Wilson-loop operator:

$$\begin{aligned} \hat{T}_+V(\boldsymbol{G}_z)\hat{W}_{2\pi,0}(3)\hat{T}_+^{-1} &= V(-\boldsymbol{G}_z)\hat{W}_{-2\pi,0}(3) \\ &= \hat{W}_{0,2\pi}(3)V(-\boldsymbol{G}_z). \end{aligned} \tag{B34}$$

To simplify our notation, we henceforth drop the constant labels for the glide index η and the quasimomentum parameter $t = 3$ [e.g., $\tilde{u}^\eta_{\alpha,(3,k_z)} \to \tilde{u}_{\alpha,k_z}$, $\mathcal{B}^\eta(3, k_z) \to \mathcal{B}(k_z)$]. Since $\hat{T}_+$ is antiunitary and squares to -1, $\hat{T}_+|\tilde{u}^\eta_{\alpha,0}\rangle \in \mathcal{B}(0)$ is orthogonal to $|\tilde{u}_{\alpha,0}\rangle$. We would further show that $\hat{T}_+|\tilde{u}_{\alpha,0}\rangle$ diagonalizes the gauge-independent Wilson loop with the same eigenvalue as $|\tilde{u}_{\alpha,0}\rangle$:

$$\begin{aligned} V(\boldsymbol{G}_z)\hat{W}_{2\pi,0}\hat{T}_+|\tilde{u}_{n,0}\rangle &= \hat{T}_+\hat{W}_{0,2\pi}V(-\boldsymbol{G}_z)|\tilde{u}_{n,0}\rangle \\ &= \hat{T}_+e^{-i\theta_n}|\tilde{u}_{n,0}\rangle \\ &= e^{i\theta_n}\hat{T}_+|\tilde{u}_{n,0}\rangle. \end{aligned} \tag{B35}$$

In the second equality, we applied Eq. (B34) and in the third Eq. (B32). Applying Eq. (B31) and (B33),

$$\hat{T}_+\big|\tilde{u}_{n,k_z}\big\rangle = e^{ik_z\theta_n/2\pi}\hat{W}_{-k_z,0}\hat{T}_+|\tilde{u}_{\alpha,0}\rangle. \tag{B36}$$

Thus if we relabel

$$\begin{aligned} \big|\tilde{u}_{\alpha,k_z}\big\rangle &:= \big|\tilde{u}_{n,k_z}\big\rangle, \\ \big|\tilde{u}_{\bar{\alpha},-k_z}\big\rangle &:= \hat{T}_+\big|\tilde{u}_{n,k_z}\big\rangle, \\ e^{i\theta_\alpha} = e^{i\theta_{\bar{\alpha}}} &:= e^{i\theta_n}, \end{aligned} \tag{B37}$$

Eqs. (B35) and (B36) may be expressed as two of the three maximally-localized conditions:

$$\begin{aligned} V(\boldsymbol{G}_z)\hat{W}_{2\pi,0}|\tilde{u}_{\bar{\alpha},0}\rangle &= e^{i\theta_{\bar{\alpha}}}|\tilde{u}_{\bar{\alpha},0}\rangle, \\ |\tilde{u}_{\bar{\alpha},k_z}\rangle &= e^{-ik_z\theta_{\bar{\alpha}}/2\pi}\hat{W}_{k_z,0}|\tilde{u}_{\bar{\alpha},0}\rangle, \end{aligned} \tag{B38}$$

and the third condition (Bloch periodicity) is simple to show. By assumption, $\tilde{u}_{\alpha,k_z}$ is also maximally localized. By construction, each pair of $\{\tilde{u}_{\alpha,k_z}, \tilde{u}_{\bar{\alpha},k_z}\}$ satisfies the time-reversal constraint [Eq. (B5)]. ■

It is instructive to compare the respective gauge conditions that have been imposed to ensure that Eq. (B7) and Eq. (B28) are well-defined $\mathbb{Z}_4$ quantities. The time-reversal condition of Eq. (B5) implies

$$i\langle\tilde{u}_{\alpha,\boldsymbol{k}}|\nabla_{\boldsymbol{k}}\tilde{u}_{\alpha,\boldsymbol{k}}\rangle = i\langle\tilde{u}_{\bar{\alpha},\boldsymbol{k}}|\nabla_{\boldsymbol{k}}\tilde{u}_{\bar{\alpha},\boldsymbol{k}}\rangle|_{\boldsymbol{k}\to-\boldsymbol{k}}, \tag{B39}$$

which ensures the pairwise-degeneracy condition on Eq. (B28):

$$i\int_{\mathcal{L}}\langle\tilde{u}_{\alpha,\boldsymbol{k}}|\nabla_{\boldsymbol{k}}\tilde{u}_{\alpha,\boldsymbol{k}}\rangle \cdot d\boldsymbol{k} := \theta_\alpha = \theta_{\bar{\alpha}} := i\int_{\mathcal{L}}\langle\tilde{u}_{\bar{\alpha},\boldsymbol{k}}|\nabla_{\boldsymbol{k}}\tilde{u}_{\bar{\alpha},\boldsymbol{k}}\rangle \cdot d\boldsymbol{k}. \tag{B40}$$

The above equality is strict and is a stronger condition than the equivalence modulo 2π [which was proven earlier in Eq. (B37)].

Combining the results of this section with Eq. (B27), we finally complete the proof of equivalence between Eq. (1) and Eq. (B3). Having proven this equivalence in the maximally-localized and time-reversal-symmetric gauge, we emphasize that the computation of the Zak phase factors $\{e^{i\theta^\eta_n}\}$ is manifestly gauge invariant; these phase factors are obtained from diagonalizing the gauge-independent Wilson loop in Eq. (B12).

APPENDIX C: TWO SYMMETRY CLASSES OF SOLIDS WITH GLIDE SYMMETRY

We introduce here two symmetry classes (labelled I and II) of solids with glide symmetry. The practical value of distinguishing these classes is that in class II, the weak $\mathbb{Z}_2$ invariant is always trivial; while the strong $\mathbb{Z}_4$ classification holds for both classes, in class II a nonprimitive unit cell must be chosen to compute the strong $\mathbb{Z}_4$ invariant.

The two classes are distinguished by the representation of glide symmetry in the Brillouin zone (BZ), which is defined standardly as the Wigner-Seitz cell of the reciprocal lattice. Glide-invariant planes in the BZ are of two types: in an *ordinary glide plane*, each wave vector $\boldsymbol{k}$ is mapped to itself by glide. In a *projective glide plane*, each $\boldsymbol{k}$ is mapped by glide to a distinct wave vector $(g_x \circ \boldsymbol{k})$ on said plane, such that $g_x \circ \boldsymbol{k}$ is translated from $\boldsymbol{k}$ by half a reciprocal vector. This is analogous to a nonsymmorphic symmetry whose fractional translation (traditionally defined in real space) now acts in $\boldsymbol{k}$ space; this analogy is elaborated on precisely in Ref. [2].

Class-I glide-symmetric solids are defined to have two ordinary glide planes in the BZ, as exemplified by $\mathrm{Ba_2Pb}$ (space group 62). For a glide symmetry g_x that inverts the wave number k_x, the two planes lie at $k_x = 0$ and $k_x = \pi/R_1$, where $2\pi\vec{x}/R_1$ is a primitive reciprocal vector. In this class, the strong $(\chi^+ \in \mathbb{Z}_4)$ and weak $(\mathcal{P}_{01} \in \mathbb{Z}_2)$ invariants may independently assume any values, as representatively illustrated in Fig. 3; this is consistent with a K-theoretic classification of surface states in Ref. [3]. We remind the reader that $\mathcal{P}_{01}$ is a Kane-Mele invariant defined over the off-center glide plane. $\mathrm{Ba_2Pb}$ falls into the $(\chi^+, \mathcal{P}_{01}) = (3, 0)$ class, as may be verified by its Zak phases in Fig. 5(a).

Class-II solids are defined to have only a single ordinary glide plane (containing the BZ center) in the BZ; an off-center glide plane exists but is projective. For a glide symmetry g_x that inverts the wave number k_x, though an off-center glide plane exists at $k_x = \pi/R_1$, $2\pi\vec{x}/R_1$ is a *not* primitive reciprocal vector; however, the existence of primitive vectors $2\pi\vec{x}/R_1 + \pi\vec{z}/R_3$ and $2\pi\vec{z}/R_3$ ensure that glide-related states in the plane are separated by half a reciprocal vector $(\pi\vec{z}/R_3)$. Consequently, the Kane-Mele invariant for the off-center glide plane is always trivial $(\mathcal{P}_{01} = 0)$, as was proven in the Appendix of Ref. [1]; see also the *reductio ad absurdum* argument through Wilson-loop connectivities in Ref. [2].

There remains for class-II solids a $\mathbb{Z}_4$ strong classification, as exemplified by KHgSb [SG D_{6h}^4; $\chi^+ = 2$; Fig. 5(b)] and uniaxially stressed $\mathrm{Na_3Bi}$ [$\chi^+ = 1$; Fig. 5(c)]. The $\mathbb{Z}_4$ invariant [cf. Eq. (1)] is only well defined for $\boldsymbol{k}$ in a modified BZ (denoted BZ') wherein both glide planes are ordinary. To appreciate this, consider that a Bloch state with wave vector $\boldsymbol{k}$ in a projective glide plane does not transform in either of the glide representations $\Delta_\pm$ (due to the glide-related states lying at inequivalent wave vectors). The simplest choice for BZ' would correspond to a nonprimitive real-space unit cell that is consistent with a glide-symmetric surface termination, as exemplified (for KHgSb) by the orange rectangle in Fig. 7(a). We remind the reader that a nonprimitive cell has larger volume than the primitive cell; it is a region that, when translated through a *subset* of vectors of the Bravais lattice, just fills all of space without overlapping itself or leaving voids [78]; the subset of vectors in our example is generated by $\boldsymbol{R}_1'$ and $\boldsymbol{R}_2'$ [Fig. 7(a)]. This subset of vectors forms a reduced Bravais lattice (denoted BL') that is distinct from the original. BZ' would then be the Wigner-Seitz cell of the reciprocal lattice dual to BL'; both BZ and BZ' of KHgSb are illustrated, respectively, as the hexagon and orange rectangle in Fig. 7(b). This prescription of enlarging the unit cell was first suggested in Ref. [3] to establish a connection between their K-theoretic classification and the material class of KHgSb. The utility of BZ' is that the $\mathbb{Z}_4$ invariant may be calculated by diagonalizing a family of Wilson loops (over the nontrivial cycles of BZ'), as was described in Sec. II A; an example of such a Wilson loop is illustrated with triple arrows in Eq. (7b). The result of this calculation for KHgSb has been shown in Fig. 5(b), from which we conclude $\chi^+ = 2$.

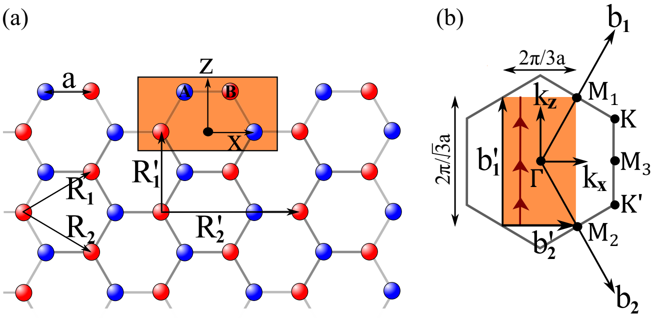

FIG. 7. (a) Constant-y cross section of the crystal structure of KHgSb, with bulk Bravais lattice vectors $\boldsymbol{R}_1$ and $\boldsymbol{R}_2$. The top armchair edge is the cross section of a glide-symmetric surface. A nonprimitive unit cell consistent with a glide-symmetric surface contains four atoms in both A and B sublattices (colored red and blue, respectively); this nonprimitive cell, when translated by vectors $\boldsymbol{R}_1'$ and $\boldsymbol{R}_2'$, covers the entire xz plane. Note that this nonprimitive unit cell has twice the volume of the primitive cell. (b) The hexagon illustrates the constant-k_z cross section of the BZ; $\boldsymbol{b}_1$ and $\boldsymbol{b}_2$ are primitive reciprocal vectors dual to $\boldsymbol{R}_1$ and $\boldsymbol{R}_2$; the orange rectangle inscribed in the hexagon illustrates BZ', which is the Wigner-Seitz cell of a modified reciprocal lattice with basis vectors $\boldsymbol{b}_1'$ and $\boldsymbol{b}_2'$ (which are dual to $\boldsymbol{R}_1'$ and $\boldsymbol{R}_2'$).

APPENDIX D: MATERIAL ANALYSIS: SPACE GROUPS AND ELEMENTARY BAND REPRESENTATIONS

1. $\mathrm{Ba_2Pb}$

The space group of $\mathrm{Ba_2Pb}$ is SG62 (*Pnma*), which has an orthorhombic lattice. The spatial symmetries include: an inversion $(\mathcal{I})$, three screws $(\{C_{2x}|\frac{1}{2}\frac{1}{2}\frac{1}{2}\}$, $\{C_{2y}|0\frac{1}{2}0\}$, and $\{C_{2z}|\frac{1}{2}0\frac{1}{2}\})$, two glide $(g_x \equiv \{r_x|\frac{1}{2}\frac{1}{2}\frac{1}{2}\}$ and $g_z \equiv \{r_z|\frac{1}{2}0\frac{1}{2}\})$, and one mirror $(\{r_y|0\frac{1}{2}0\})$. Note r_j is a mirror operation that inverts the single coordinate j.

For the calculations of topological invariants, we redefine the lattice vectors as $\vec{a}' = 2\vec{a} + \vec{b}$, $\vec{b}' = b$, and $\vec{c}' = c$, which

TABLE I. Irreducible representations for Ba2Pb, as computed by VASP.

	Valence bands
Γ	6;5;6;5;5;6;5;6;6;5;6;6;
R	$4+4$;$3+3$;$3+3$;$4+4$;$3+3$;$4+4$;
S	$4+4$;$3+3$;$3+3$;$4+4$;$4+4$;$3+3$;
T	$3+4$;$3+4$;$3+4$;$3+4$;$3+4$;$3+4$;
U	$5+5$;$6+6$;$6+6$;$5+5$;$6+6$;$5+5$;
X	$3+4$;$3+4$;$3+4$;$3+4$;$3+4$;$3+4$;
Y	$3+4$;$3+4$;$3+4$;$3+4$;$3+4$;$3+4$;
Z	$3+4$;$3+4$;$3+4$;$3+4$;$3+4$;$3+4$;

are orthogonal. We can then set a', b', and c' as the x, y, z axes. With respect to these new lattice vectors, the glide symmetry is represented by $g_x \equiv \{r_x|00\frac{1}{2}\}$.

Beside exhibiting a nontrivial connectivity of the Zak phases [cf. Fig. 5(a)], another manifestation [21,62] of the nontriviality of $\mathrm{Ba_2Pb}$ is that its ground state is not a direct sum of elementary band representations [21,62]. To prove this, it is sufficient to compare the irreducible representations (irreps) at high-symmetry wave vectors [21,120]. By inspection, the irreps of $\mathrm{Ba_2Pb}$ (Table I) cannot be decomposed into a direct sum of irreps of the elementary band representations, as obtained from the Bilbao crystallographic server (reproduced in Table II).

2. Stressed $\mathrm{Na_3Bi}$

For $\mathrm{Na_3Bi}$ that is stressed in the x direction, the space group falls into *Cmcm* (SG 63), which is a body-center structure. The conventional lattices are redefined as $\vec{a}' = 0.98(\vec{a}+\vec{b})$ where the factor 0.98 is due to a hypothetical compression in the x direction, $\vec{b}' = b$ and $\vec{c}' = c$, where a, b, c are the primitive lattice vectors in the original structure(SG 194). χ^+ is calculated with the conventional (nonprimitive) lattices. The glide symmetry is represented by $g_x \equiv \{r_x|00\frac{1}{2}\}$. By comparing the irreps of all elementary band representations (in SG63; see Table III) with the irreps of stressed $\mathrm{Na_3Bi}$ (cf. Table IV), we conclude that the ground state of stressed $\mathrm{Na_3Bi}$ is not band representable.

3. KHgSb

The space group of KHgSb is D^4_{6h} or SG194; further details about its crystallographic structure may be found in Ref. [1]. By comparing the irreps of all elementary band representations (in SG194; see Table V) with the irreps of KHgSb (cf. Table VI), we conclude that the ground state of KHgSb is not band representable.

APPENDIX E: AMBIGUITY IN THE CHOICE OF COORDINATE SYSTEMS

This Appendix addresses a question posed at the end of Sec. IV, which we will briefly recapitulate. Suppose we choose a right-handed, Cartesian coordinate system where $\vec{\boldsymbol{x}}$ (resp. $\vec{\boldsymbol{y}}$) lies parallel to the reflection (resp. fractional translational) component of the glide, i.e., the glide maps $(x, y, z) \rightarrow (-x, y \pm R_2/2, z)$. Such a coordinate system would be called glide symmetric. Would the topological invariants χ^+ (or $\mathcal{C}$) differ if measured in distinct glide-symmetric coordinates?

As argued in Sec. IV, there are three glide-symmetric coordinates which are related to each other by twofold rotations C_{2j} about the directional axes $\vec{j}$ $(j = x, y, z)$; we shall only concern ourselves with proper point-group transformations that preserve the orientation (or handedness) of the coordinate system. We will refer to one glide-symmetric, right-handed (but otherwise arbitrarily chosen) coordinate system—in $\boldsymbol{k}$ space—as the *reference coordinate system*; all other coordinate systems are related to the reference by $\boldsymbol{k}' = p \circ \boldsymbol{k}$, with p a point-group transformation [e.g., $C_{2x} \circ \boldsymbol{k} := (k_x, -k_y, -k_z)$ etc.]. It should be emphasized that p is *not necessarily* a symmetry of the solid (i.e., not an element of the space group) but merely reflects an ambiguity in the choice of coordinates.

To establish notation, a map between points: $\boldsymbol{k} \rightarrow p \circ \boldsymbol{k}$ induces naturally a map between subregions of the Brillouin torus (e.g., lines denoted as l, or faces denoted as a, b, c, d.); we shall denote this as $l \rightarrow p \circ l$ etc; several examples are illustrated in Fig. 8. It is useful (as an intermediate step in the following computations) to decompose C_{2x} as the product of two reflections r_y and r_z, such that each r_j inverts only the jth coordinate $(j = x, y, z)$. We will also consider coordinate transformations induced by the inversion $\mathcal{I} : (x, y, z) \rightarrow (-x, -y, -z)$, though inversion symmetry need not belong in the space group. We separately analyze the coordinate dependence of $\mathcal{C}$ and $\chi^{\pm}$ in Appendix E 1 and Appendix E 2, respectively.

TABLE II. Elementary band representations [21,120] for SG62.

Wyckoff pos. Band-rep.	4a A_gA_g	4a A_uA_u	4b A_gA_g	4b A_uA_u	4c $^1E^2E$
Γ	4×5	4×6	4×6	4×6	4×6
R	$(3+3)\oplus(4+4)$	$(3+3)\oplus(4+4)$	$(3+3)\oplus(4+4)$	$(3+3)\oplus(4+4)$	$(3+3)\oplus(4+4)$
S	$(3+3)\oplus(4+4)$	$(3+3)\oplus(4+4)$	$(3+3)\oplus(4+4)$	$(3+3)\oplus(4+4)$	$(3+3)\oplus(4+4)$
T	$2\times(3+4)$	$2\times(3+4)$	$2\times(3+4)$	$2\times(3+4)$	$2\times(3+4)$
U	$2\times(5+5)$	$2\times(6+6)$	$2\times(6+6)$	$2\times(5+5)$	$(5+5)\oplus(6+6)$
X	$2\times(3+4)$	$2\times(3+4)$	$2\times(3+4)$	$2\times(3+4)$	$2\times(3+4)$
Y	$2\times(3+4)$	$2\times(3+4)$	$2\times(3+4)$	$2\times(3+4)$	$2\times(3+4)$
Z	$2\times(3+4)$	$2\times(3+4)$	$2\times(3+4)$	$2\times(3+4)$	$2\times(3+4)$

TABLE III. Elementary band representations for SG63.

Wyckoff pos. Band-rep.	4a ${}^1E_g^2E_g$	4a ${}^1E_u^2E_u$	4b ${}^1E_g^2E_g$	4b ${}^1E_u^2E_u$	4c E
Γ	2×5	2×6	2×5	2×6	$5+6$
R	$2+2$	$2+2$	$2+2$	$2+2$	$2+2$
S	$2\times(3+4)$	$2\times(5+6)$	$2\times(5+6)$	$2\times(3+4)$	$(3+4)\oplus(5+6)$
T	$3+4$	$3+4$	$3+4$	$3+4$	$3+4$
Y	2×5	2×6	2×5	2×6	$5+6$
Z	$3+4$	$3+4$	$3+4$	$3+4$	$3+4$

1. Coordinate dependence of the bent Chern number $\mathcal{C}$

We begin by defining the Berry curvature as a pseudovector field $\boldsymbol{\mathcal{F}}=(\mathcal{F}_x,\mathcal{F}_y,\mathcal{F}_z)$, with components

$$\mathcal{F}_a = i\epsilon_{abc}\sum_{n=1}^{n_{\rm occ}}\langle\partial_b u_n|\partial_c u_n\rangle; \tag{E1}$$

∂_j is shorthand for the derivative with respect to k_j, ϵ_{abc} is the Levi-Cevita tensor, repeated indices (e.g., b, c above) are summed over the Cartesian directions x, y, z. The bent Chern number is defined as the integral of the Berry curvature

$$\mathcal{C} = -\int_{|a|}\mathcal{F}_x dk_y dk_z - \int_{|b|}\mathcal{F}_y dk_x dk_z + \int_{|c|}\mathcal{F}_x dk_y dk_z + \int_{|d|}\mathcal{F}_y dk_x dk_z, \tag{E2}$$

where $|f|$ in the subscript of $\int_{|f|}$ denotes the face f without its orientation. The $\pm$ signs in front of each integral reflect our convention that $\mathcal{C}$ measures the outgoing Berry 'flux,' or equivalently the net charge of the Berry monopoles within the quadrant enclosed by $abcd$. An equivalent and useful expression is

$$\mathcal{C} = \frac{i}{2\pi}\int_0^4\frac{dt}{4}\int_0^{2\pi}\frac{dk_z}{2\pi}\left[\left\langle\partial_t u\middle|\partial_{k_z}u\right\rangle - \left\langle\partial_{k_z}u\middle|\partial_t u\right\rangle\right], \tag{E3}$$

where $t\in[0,4]$ (with $4\equiv 0$) parametrizes the loop l on which $abcd$ projects in the z direction, as illustrated in Fig. 8(a) [see also Fig. 2(b)]. l is anticlockwise oriented [as indicated by arrows in Fig. 8(a)], and t increases in the direction of the orientation loop l.

Let $\mathcal{C}$ be the Chern number defined over $abcd$ in the reference coordinate system (parametrized by $\boldsymbol{k}$). We define $p\circ\mathcal{C}$ as the same Chern number in a different coordinate system parametrized by $\boldsymbol{k}'=p\circ\boldsymbol{k}$; that is, $p\circ\mathcal{C}$ is defined exactly as in Eq. (E2) but with $\boldsymbol{k}$ replaced by $\boldsymbol{k}'$. For the same Hamiltonian, we would prove that

$$\mathcal{C} = r_x\circ\mathcal{C} = r_y\circ\mathcal{C} = -r_z\circ\mathcal{C}. \tag{E4}$$

TABLE IV. Irreducible representations for stressed Na3Bi, as computed by VASP.

	Valence bands
Γ	5;6;5;5;5 + 6;
R	8; 12; 11; 9; 8; 12;
S	5 + 6; 3 + 4; 3 + 4; 5 + 6; 3 + 4; 5 + 6;
T	3 + 4; 3 + 4; 3 + 4;
Y	5; 6; 6; 5; 6; 5;
Z	3 + 4; 3 + 4; 3 + 4;

To prove the first equality, consider that $r_x\circ\mathcal{C}$ is the Chern number defined over $a'b'c'd'=r_x\circ abcd$ in the $\boldsymbol{k}'=(-k_x,k_y,k_z)$ coordinates, as illustrated in Fig. 8(c). In the reference coordinates, $a'b'c'd'$ is comparatively illustrated with $abcd$ in Fig. 8(b). Since $a'b'c'd'$ and $abcd$ are related by the reflection r_x, they enclose different quadrants of the BZ (colored red and blue, respectively). To deduce that $\mathcal{C}=r_x\circ\mathcal{C}$, we will rely on two observations: (i) While $r_x\circ\mathcal{C}$ is defined to measure the outgoing Berry flux in the $\boldsymbol{k}'$ coordinates, it measures the incoming Berry flux in the reference coordinates $\boldsymbol{k}$; this may be deduced by the $r_x\circ l$ having an opposite orientation relative to l, as illustrated in Figs. 8(a) and 8(b). (ii) Since the curvature transforms like a pseudovector, we expect that glide-related Berry monopoles have opposite charge—therefore the net monopole charge in the blue quadrant is negative the monopole charge in the red quadrant. In combination, (i)–(ii) produces the desired result.

$\mathcal{C}=r_y\circ\mathcal{C}$ [the second equality in Eq. (E4)] may be derived by a simple generalization of the above argument. Now the two quadrants (enclosed by $abcd$ and $r_y\circ abcd$) are related by a composition (Tg_x) of time-reversal and glide symmetry. (i′) $r_y\circ\mathcal{C}$ also measures the incoming Berry flux in the reference coordinates, and (ii′) Tg_x-related monopoles have opposite charge. (Note that r_y is not assumed be a symmetry in the space group, but if it were, we would similarly conclude that r_y-related monopoles have opposite charge).

$\mathcal{C}=-r_z\circ\mathcal{C}$ [the last equality in Eq. (E4)] may be derived from the following argument. When both $abcd$ and $a'b'c'd'=r_z\circ abcd$ are viewed in the reference coordinates, the two surfaces occupy the same area (in $\boldsymbol{k}$ space) and differ only in their orientations; this difference in orientations originates from the reversal of k_z. This implies that $r_z\circ\mathcal{C}$ measures the *incoming* Berry flux through $abcd$. From Eq. (E4) and $C_{2x}=r_yr_z$ etc., we derive that the bent Chern numbers—for two coordinate parametrizations of the same Hamiltonian—are related as

$$p\circ\mathcal{C} = \begin{cases} -\mathcal{C}, & p\in\{C_{2x},C_{2y}\},\\ \mathcal{C}, & p=C_{2z}.\end{cases} \tag{E5}$$

2. Coordinate dependence of topological invariant $\chi^{\pm}$

Let us define $\chi^{\pm}$ as $\mathbb{Z}_4$ invariants defined with respect to a reference coordinate system parametrized by $\boldsymbol{k}$; analogously,

TABLE V. Elementary band representations for SG194

Wyckoff pos.	2a	2a	2a	2a	2b	2b	2b	2c	2c	2c	2d	2d	2d
Band-rep.	${}^1E_g^2E_g$	${}^1E_u^2E_u$	E_{1g}	E_{1u}	E_1	E_2	E_3	E_1	E_2	E_3	E_1	E_2	E_3
A	$(4+5)$	$(4+5)$	6	6	6	6	$4+5$	6	6	$4+5$	6	6	$4+5$
Γ	2×7	2×10	$8\oplus 9$	$11\oplus 12$	$9\oplus 11$	$8\oplus 12$	$7\oplus 10$	$9\oplus 11$	$8\oplus 12$	$7\oplus 10$	$9\oplus 11$	$8\oplus 12$	$7\oplus 10$
H	$(4+5)\oplus(6+7)$	$(4+5)\oplus(6+7)$	$8\oplus 9$	$8\oplus 9$	$8\oplus 9$	$8\oplus 9$	$(4+5)\oplus(6+7)$	$(4+5)\oplus 9$	$(6+7)\oplus 8$	$8\oplus 9$	$(4+5)\oplus 9$	$(6+7)\oplus 8$	$8\oplus 9$
K	2×7	2×7	$8\oplus 9$	$8\oplus 9$	2×9	2×8	2×7	$7\oplus 8$	$7\oplus 9$	$8\oplus 9$	$7\oplus 8$	$7\oplus 9$	$8\oplus 9$
L	$3+4$	$3+4$	$3+4$	$3+4$	$3+4$	$3+4$	$3+4$	$3+4$	$3+4$	$3+4$	$3+4$	$3+4$	$3+4$
M	2×5	2×6	2×5	2×6	$5+6$	$5+6$	$5+6$	$5+6$	$5+6$	$5+6$	$5+6$	$5+6$	$5+6$

$p\circ\chi^{\pm}$ are defined as the $\mathbb{Z}_4$ invariants defined with respect to a distinct coordinate system with $\boldsymbol{k}'=p\circ\boldsymbol{k}$. For the same Hamiltonian, we will show that

$$p\circ\chi^{\pm}=\begin{cases}-\chi^{\mp}, & p\in\{C_{2x},C_{2y}\},\\ \chi^{\pm}, & p=C_{2z}.\end{cases}\tag{E6}$$

This would imply, in combination with Eq. (E5), that $\chi^{+}+\chi^{-}\equiv 2\mathcal{C}$ mod 4 [cf. Eq. (4)] is invariant under proper coordinate transformations—a result applicable to both band insulators and Weyl metals.

The rest of this Appendix is devoted to proving Eq. (E6). Let l be the oriented path in (k_x,k_y) space on which $\chi^{\pm}[l]$ is defined through Eq. (1). l is illustrated in Fig. 9(a), in conjunction with the three other point-group mapped $p\circ l$; we remind the reader that p is not necessarily a symmetry of the solid. A word of caution: l was also used in the previous section to define a loop illustrated in Fig. 8; in this section we use the same symbol l for an open segment of the loop in Fig. 8.

For each of $p\circ l$ illustrated in Fig. 9(a), we define the quantities $\chi^{\pm}[p\circ l]$ which simply generalize our original definition in Eq. (1):

$$\begin{aligned}\chi^{\pm}[p\circ l]=\frac{1}{\pi}\sum_{j=1}^{n_{\rm occ}/2}&\bigg[\theta_j^{\pm}[p\circ l(0)]-\theta_j^{\pm}[p\circ l(3)]\\&+\int_{[p\circ l(0)]}^{[p\circ l(1)]}d\theta_j^{\pm}+\int_{[p\circ l(2)]}^{[p\circ l(3)]}d\theta_j^{\pm}\bigg]\\&+\frac{1}{2\pi}\sum_{j=1}^{n_{\rm occ}}\int_{[p\circ l(1)]}^{[p\circ l(2)]}d\theta_j.\end{aligned}\tag{E7}$$

Equation (1) is a particularization of $\chi^{\pm}[p\circ l]$ for p being the identity operation. Here, we have parametrized $p\circ l(t)$ by $t\in[0,3]$ such that $t\in\{0,1,2,3\}$ lie on the high-symmetry wave vectors in the k_x-k_y plane, as illustrated in Fig. 9(a). $\{e^{i\theta_j[p\circ l(t)]}\}$ are eigenvalues of the Wilson loop—for an oriented quasimomentum loop which projects in the z direction to the wave vector $p\circ l(t)$, as illustrated by the triple arrows in Fig. 9(b); by definition, the orientation of each loop is always in the direction of increasing k_z.

In congruence with our previous definitions, $\chi^{\pm}[p_1\circ l]$ is defined with respect to a reference coordinate $\boldsymbol{k}$, and we define $p_2\circ\chi^{\pm}[p_1\circ l]$ with respect to $\boldsymbol{k}'=p_2\circ\boldsymbol{k}$, with p_1 not necessarily equal to p_2. We caution that $\chi^{\pm}[p\circ l]$ and $p\circ\chi^{\pm}[l]$ are not necessarily equal, as will be seen in Eq. (E16).

TABLE VI. Irreducible representations for KHgSb, as computed by VASP.

	Valence bands
A	6;6;6;
Γ	8;12; 11; 9; 8; 12;
H	6 + 7; 8; 9; 8; 6 + 7; 8;
K	7; 8; 9; 9; 7; 9;

a. Proposition 1

Let us prove an intermediate proposition:

$$\chi^{\pm}[l]\equiv\chi^{\pm}[r_x\circ l]\equiv\chi^{\mp}[r_y\circ l]\equiv\chi^{\mp}[C_{2z}\circ l],\tag{E8}$$

where $\equiv$ is an equivalence modulo four. Let us introduce the shorthand $p\circ j(j+1)$, for $j\in\{0,1,2\}$, as the subset of $p\circ l(t)$ in which $t\in[j,j+1]$. That is, l is the union of intervals 01, 12, and 23, and so similarly we define $p\circ 01$, $p\circ 12$ and $p\circ 23$ for $p\circ l$. The relation in Eq. (2) simply generalizes to

$$\chi^{\pm}[p\circ l]\equiv 2\mathcal{S}^{\pm}_{p\circ 01}(\bar\theta)+\mathcal{S}_{p\circ 12}(\bar\theta)+2\mathcal{S}^{\pm}_{p\circ 23}(\bar\theta),\tag{E9}$$

where $\mathcal{S}_{p\circ ij}$ is defined analogously to $\mathcal{S}_{ij}$, as introduced in the main text. We write it down for clarity: draw a constant-$\bar\theta$ reference line (for an arbitrarily chosen Zak phase $\bar\theta$) and consider its intersections with Zak bands along $p\circ l$. For each intersection between $p\circ 12$, we calculate the sign of the velocity $d\theta/dt$ and sum this quantity over all intersections to obtain $\mathcal{S}_{p\circ 12}(\bar\theta)$; for $p\circ 01$ and $p\circ 23$, we consider only intersections with Zak bands in the $\Delta_{\pm}$ representation, and we similarly sum over sgn$[d\theta/dt]$ to obtain $\mathcal{S}^{\pm}_{p\circ 01}(\bar\theta)$ and $\mathcal{S}^{\pm}_{p\circ 23}(\bar\theta)$, respectively.

Proof of $\chi^{\pm}[l]\equiv\chi^{\pm}[r_x\circ l]$.

Along the glide-invariant lines, $r_x\circ 01=01$ and $r_x\circ 23=23$, and therefore $\mathcal{S}^{\pm}_{r_x\circ 01}=\mathcal{S}^{\pm}_{01}$ and $\mathcal{S}^{\pm}_{r_x\circ 23}=\mathcal{S}^{\pm}_{23}$. However, $r_x\circ 12\neq 12$ lie on distinct lines which are related by time-reversal symmetry [which maps $(k_x,k_y)\to(-k_x,-k_y)$], as illustrated in Fig. 9(a). This symmetry imposes $\mathcal{S}_{12}=\mathcal{S}_{r_x\circ 12}$, as we now explain. Suppose a Zak band over 12 intersects our constant-$\bar\theta$ line with velocity v, then its time-reversed partner is a Zak band over $r_x\circ 12$, which intersects the $\bar\theta$ line with velocity $-v$. By v and $-v$, we refer to velocities defined by varying the Zak phase of a Zak band with respect to k_x. However, our definition of $\mathcal{S}_{p\circ ij}$ involved velocities defined by varying the Zak phase with respect to a parameter that is specific to $p\circ ij$: The parameter for 12 increases in the same direction as k_x, but the parameter for $r_x\circ 12$ increases in the opposite direction, as illustrated in Figs. 9(a) and 9(d). Therefore, each pair of time-reversed Zak bands contribute equally to $\mathcal{S}_{12}$

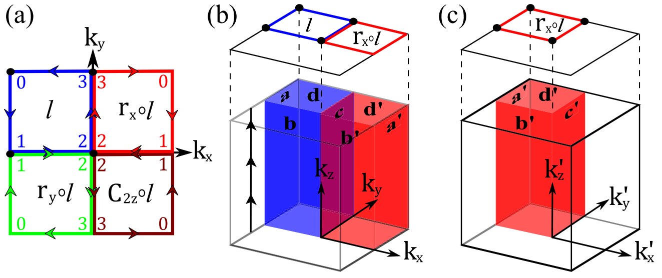

FIG. 8. (a) Illustration of $p\circ l$ in the surface Brillouin torus. (b) Bent manifolds *abcd* and $a'b'c'd' = r_x\circ abcd$ in the $\boldsymbol{k}$ coordinates; note that $r_x\circ c$ and c differ only in orientation. (c) $r_x\circ abcd$ in the reflected coordinates $(k_x', k_y', k_z') = (-k_x, k_y, k_z)$.

and $\mathcal{S}_{r_x\circ 12}$, leading to $\mathcal{S}_{12} = \mathcal{S}_{r_x\circ 12}$. For example, consider a representative Zak-band dispersion in Fig. 9(d), where $\mathcal{S}_{12} = \mathcal{S}_{r_x\circ 12} = 2$ for the chosen reference line (colored orange). ■

Proof of $\chi^{\pm}[l] \equiv \chi^{\mp}[r_y\circ l]$.

Since $12 = r_y\circ 12$,

$$\mathcal{S}_{12} = \mathcal{S}_{r_y\circ 12}. \tag{E10}$$

Time reversal relates 01 and $r_y\circ 01$ and therefore imposes a relation between $\mathcal{S}^{\pm}_{01}$ and $\mathcal{S}^{\pm}_{r_y\circ 01}$, as we now derive. Recall from Appendix A 2 that time-reversed partner states at $\pm k_y$ belong to opposite representations $\Delta_{\pm}$ of the glide g_x. This implies that (a) a Zak band in the $\Delta_{\pm}$ representation at 01 has a time-reversed partner at $r_y\circ 01$ in the $\Delta_{\mp}$ representation; note that 01 and $r_y\circ 01$ are distinct lines in $\boldsymbol{k}$ space. (b) Moreover, as representatively illustrated in Fig. 9(e), time-reversed partners have opposite-sign velocities with respect to variation of k_y but equal velocities with respect to varying the parameters of 01 and $r_y\circ 01$, respectively. (a) and (b) together imply

$$\mathcal{S}^{\pm}_{01} = \mathcal{S}^{\mp}_{r_y\circ 01}. \tag{E11}$$

By cosmetic substitution of 12 → 23 in the above demonstration, we would show that

$$\mathcal{S}^{\pm}_{23} = \mathcal{S}^{\mp}_{r_y\circ 23}. \tag{E12}$$

Eq. (E10), Eq. (E11), Eq. (E12), and Eq. (E9) together imply our claim. ■

Finally, $\chi^{\pm}[l] \equiv \chi^{\mp}[C_{2z}\circ l]$ may be proven from

$$\mathcal{S}_{12} = \mathcal{S}_{C_{2z}\circ 12},\quad \mathcal{S}^{\pm}_{01} = \mathcal{S}^{\mp}_{C_{2z}\circ 01},\quad \mathcal{S}^{\pm}_{23} = \mathcal{S}^{\mp}_{C_{2z}\circ 23}. \tag{E13}$$

b. Dependence on proper coordinate transformations

Let the p be a proper point-group transformation that preserves handedness of the coordinate system. p can always be viewed as the composition of a two-dimensional point-group operation ($p_\perp$) acting in the $k_x - k_y$ plane and a one-dimensional point group operation acting in the k_z line:

$$p\circ\boldsymbol{k} = (p_\perp\circ(k_x,k_y),\, p_\parallel k_z),\qquad p_\parallel\in\pm 1. \tag{E14}$$

This gives a correspondence $p\leftrightarrow(p_\perp, p_\parallel)$. We are particularly interested in

$$C_{2x}\leftrightarrow(r_y,-1),\quad C_{2y}\leftrightarrow(r_x,-1),\quad C_{2z}\leftrightarrow(C_{2z},+1). \tag{E15}$$

For two coordinate parametrizations ($\boldsymbol{k}$ and $\boldsymbol{k}' = p\circ\boldsymbol{k}$) of the same Hamiltonian, we argue that

$$p\circ\chi^{\pm}[l,k_z] = \chi^{\pm p r_x p^{-1} r_x^{-1}}[p_\perp\circ l,\, p_\parallel k_z], \tag{E16}$$

where $\chi^{\pm}[p\circ l, k_z] := \chi^{\pm}[p\circ l]$ as defined in Eq. (E7), and $\chi^{\pm}[p\circ l, k_z]$ is identical to $\chi^{\pm}[p\circ l]$ except that the orientation of each Wilson loop is reversed (from increasing k_z to decreasing k_z). The above equation has the following justification:

(i) A coordinate transformation effectively changes the bent quasimomentum region on which χ is calculated; this is reflected in a change in the argument of χ. For example, $r_x\circ\chi^{\pm}[l,k_z]$ is defined over the bent quasimomentum subregion $a'b'c' = r_x\circ abc$ that we illustrate in the primed coordinates [red sheet in Fig. 9(c)] and reference coordinates [red sheet in Fig. 9(b)]; $r_x\circ abc$ projects in the z direction to $r_x\circ l$.

(ii) Whether the glide representation changes under a coordinate transformation $(x,y,z)\rightarrow(x',y',z') = p\circ(x,y,z)$ depends on p. To appreciate this, let us recall that the reflection component (r_x) of glide g_x has an associated orientation. Indeed, r_x may be viewed as the composition of a spatial inversion ($\mathcal{I}$) with the twofold rotation (C_{2x}) about the x axis, and, for *half-integer-spin representations*, we need to specify if this rotation is clockwise or anticlockwise oriented. That is to say, a π clockwise rotation differs from a π anticlockwise rotation by a -1 phase factor. Consequently, the *same* glide-invariant state has glide eigenvalues with *opposite* signs—with respect to two glide operations which differ only in orientation. For a coordinate system (x,y,z), we always define g_x with a clockwise rotation about the x axis; this was implicit

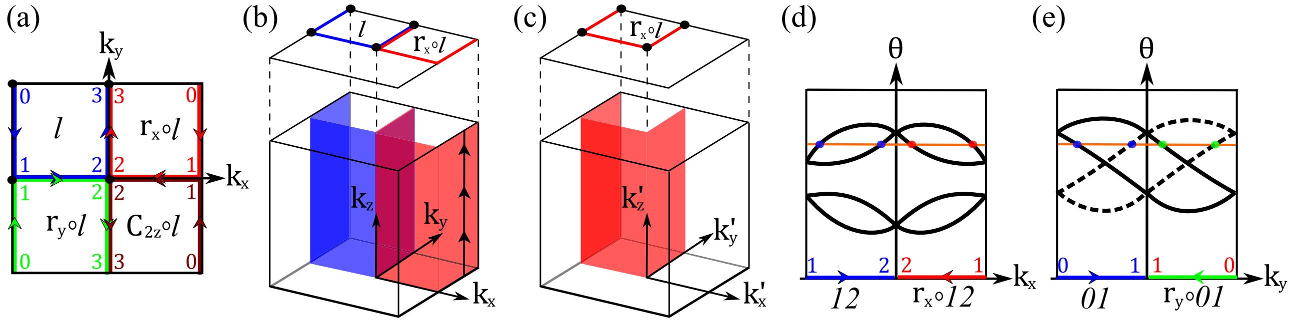

FIG. 9. (a) Illustration of $p\circ l$ in the surface Brillouin torus. (b) Bent subregions on which the $\mathbb{Z}_4$ invariants $\chi[p\circ l]$ are defined. (c) Bent subregion in which $r_x\circ\chi^{\pm}[l]$ is defined, in the reflected coordinates $(k_x', k_y', k_z') = (-k_x, k_y, k_z)$. (d) Representative Zak-phase dispersion along 12 and $r_x\circ 12$. (e) Representative Zak-phase dispersion along 01 and $r_y\circ 01$.

in our previous definitions of $\Delta_\pm$ and $\chi^\pm$. Suppose a Bloch state transforms under g_x with eigenvalue $\Delta_\pm = \pm i e^{-ik_y/2}$; the *same* state may (or may not) transform with the inverted eigenvalue $\mp i e^{-ik_y/2}$ under the glide $g_{x'}$, which is defined with a clockwise orientation about the x' axis [recall $(x', y', z') = p \circ (x, y, z)$]. The glide eigenvalue is inverted if and only if the coordinate transformation p inverts the orientation of a rotation about the x axis, i.e., it depends on $p r_x p^{-1} r_x^{-1} = \pm 1$ (with -1 indicating an inversion), for example, if $p = C_{2x}$, $g_{x'}$, and g_x have the same orientations; if $p = C_{2y}$, $g_{x'}$, and g_x have opposite orientations, then r_x and C_{2y} anticommute in the half-integer-spin representation. This possible change in the glide representation is accounted for in Eq. (E16) by the superscript of χ.

Beginning from Eq. (E16), the next step is to express

$$p \circ \chi^\pm[l, k_z] \equiv p_\parallel \chi^{\pm p r_x p^{-1} r_x^{-1}}[p_\perp \circ l, k_z]. \tag{E17}$$

To justify this, $p_\parallel = -1$ implies that the orientation of the Wilson loop flips, thus $e^{i\theta}(t) \rightarrow e^{-i\theta}(t)$, and the velocities at the reference Zak phase are likewise inverted; cf. Eq. (E9). Finally, inserting Eq. (E15) and Eq. (E8) (which should be understood as relating χ with constant k_z arguments) into Eq. (E17), we obtain

$$\begin{aligned} C_{2x} \circ \chi^\pm[l, k_z] &\equiv -\chi^\pm[r_y \circ l, k_z] \equiv -\chi^\mp[l, k_z], \\ C_{2y} \circ \chi^\pm[l, k_z] &\equiv -\chi^\mp[r_x \circ l, k_z] \equiv -\chi^\mp[l, k_z], \\ C_{2z} \circ \chi^\pm[l, k_z] &\equiv \chi^\mp[C_{2z} \circ l, k_z] \equiv \chi^\pm[l, k_z], \end{aligned} \tag{E18}$$

from which Eq. (E6) follows directly.

APPENDIX F: CONSIDERATION OF LIGHT SOURCES FOR PHOTOEMISSION

To exploit the selection rule developed in Sec. V, we would like that the electron-photon coupling H_{int} transforms in a one-dimensional representation of glide reflection [cf. Eq. (9)]. As we will show in this Appendix, this transformation holds for a linearly-polarized light source, with photon wave vector parallel to the glide-invariant yz plane and with the polarization vector $\vec{\epsilon}$ either orthogonal [see Fig. 6(d)] or parallel [Fig. 6(c)] to the glide-invariant plane. To orient $\vec{\epsilon}$ relative to the glide plane, we would need to know the sample's crystallographic orientation; this may be obtained by independent experiments (e.g., x-ray diffraction) or by comparison of the angle-resolved photoemission data to a first-principles calculation (where the glide plane is known).

For the purpose of demonstrating Eq. (9), it is useful to distinguish between normally and obliquely incident light. With oblique incidence, we identify (by standard convention) the parallel alignment as p polarization and the orthogonal alignment as s polarization, e.g., compare Figs. 6(c) and 6(d). For normal incidence, the two types of polarization are indistinguishable.

The cases of normal incidence (both parallel and orthogonal alignments) and oblique incidence (orthogonal alignment) will be dealt with in Appendix F 1, where we prove Eq. (9) within the classical approximation [66,68,81,106] of light within the solid. This classical approximation is invalid (for surface photoemission) in the case of oblique incidence (parallel alignment); nevertheless, so far as nonlinearities in the optical response (of the medium) can be neglected, we will find in Appendix F 2 that Eq. (9) still holds.

1. Normal incidence (parallel and orthogonal alignments) and oblique incidence (orthogonal alignment)

For such incidence angles and polarizations, the incident electric field is parallel to the surface, allowing for a classical, Maxwell-based approximation of the electromagnetic field (within the solid). We briefly review why: Corrections to the classical approximation are known as local fields, which are believed to be only significant near the surfaces of solids [121], where surface plasmons and electron-hole pairs may be excited by the incident radiation [66–68]. Consequently, local-field effects are especially relevant to surface photoemission, which is the main application in Sec. IV. It is known that local-field effects are negligible if the incident electric field is aligned parallel to the surface (i.e., $\vec{\epsilon}$ lies in the xy plane) [66–68,81,106]. The reason is that surface-parallel electric-field components vary smoothly across the surface, while surface-normal electric-field components can vary rapidly on the order of atomic distances (thus invalidating the dipole approximation). Even within the classical, Maxwell-based approximation, it is known that surface-normal field components are discontinuous across the interface of two distinct media due to the presence of a surface charge [122]; this surface charge is an idealization, and its proper, quantum description is given by the aforementioned surface plasmons and electron-hole pairs [68]. Within the classical approximation, and for the above-stated conditions on the light source, Fresnel's equations [122] inform us that the photon field within the solid remains linearly polarized, with a polarization vector $\vec{\epsilon}$ (within the solid) that is identical to the polarization vector of the light source.

In the temporal gauge, the electric field and vector potential are parallel, hence $\boldsymbol{a}$ (the screened vector potential within the solid) is proportional to $\vec{\epsilon}$. So far as we are concerned only with the absorption of photons, $\boldsymbol{a}$ (occurring in the electron-photon coupling H_{int}) may be equated with $a_0 \vec{\epsilon} e^{i\boldsymbol{q}\cdot\boldsymbol{r}}$, where a_0 is a spatially-independent constant, and $\boldsymbol{q}$ is the wave vector of the photon within the solid.

For normally-incident light ($\boldsymbol{q} = -\omega\vec{z}/c$) with the polarization vector parallel to the glide plane ($\epsilon = \vec{y}$), H_{int} commutes with the glide operation $\hat{g}_x$. If the polarization vector is orthogonal to the glide plane ($\vec{\epsilon} = \vec{x}$), H_{int} anticommutes with $\hat{g}_x$ in the case of normal incidence. For non-normal incidence and $\vec{\epsilon} = \vec{x}$, $\hat{g}_x H_{\text{int}} \hat{g}_x^{-1} = -e^{-iq_y R_2/2} H_{\text{int}}$; the q_y-dependent phase factor originates from the half-lattice translation ($y \rightarrow y - R_2/2$) in $\hat{g}_x$.

2. Oblique incidence (parallel alignment)

As explained in the previous Appendix F 1, the classical approximation is *not* satisfied if the incident electric field has a component normal to the surface, as would be the case for p-polarized radiation at oblique incidence [66–68]. Nevertheless, so long as the optical response of the medium is linear (though not necessarily local [68]), the electron coupling to the medium-induced electromagnetic field (given by vector potential $\boldsymbol{a}^{\text{ind}}$) transforms in the same glide representation as the electron coupling to the externally applied field (given by $\boldsymbol{a}^{\text{ext}}$) [123]. That is to say, if $\hat{g}_x \boldsymbol{p}\cdot\boldsymbol{a}^{\text{ext}}\hat{g}_x^{-1} = e^{-iq_yR_2/2}\boldsymbol{p}\cdot\boldsymbol{a}^{\text{ext}}$, so must $\hat{g}_x \boldsymbol{p}\cdot\boldsymbol{a}^{\text{ind}}\hat{g}_x^{-1} = e^{-iq_yR_2/2}\boldsymbol{p}\cdot\boldsymbol{a}^{\text{ind}}$. This follows from the assumed existence of a linear functional relating the two potentials:

$$a_i^{\text{ind}}(\boldsymbol{r}) = \sum_{j=x,y,z} \int \chi_{ij}(\boldsymbol{r},\boldsymbol{r}')a_j^{\text{ext}}(\boldsymbol{r}')d\boldsymbol{r}', \tag{F1}$$

with the susceptibility satisfying the glide-symmetric constraint:

$$\chi_{ij}(\boldsymbol{r},\boldsymbol{r}') = \sum_{a,b}[\mathfrak{r}_x]_{ia}[\mathfrak{r}_x]_{jb}\chi_{ij}(g_x\circ\boldsymbol{r}, g_x\circ\boldsymbol{r}'),$$
$$\mathfrak{r}_x := \begin{pmatrix} -1 & 0 & 0\\ 0 & 1 & 0\\ 0 & 0 & 1\end{pmatrix},\quad g_x\circ(x,y,z)$$
$$:= (-x, y-R_2/2, z). \tag{F2}$$

Consequently, the electron coupling to the *total* photon field transforms as $\hat{g}_x H_{\text{int}}\hat{g}_x^{-1} = e^{-iq_yR_2/2}H_{\text{int}}$.

[1] Z. Wang, A. Alexandradinata, R. J. Cava, and B. A. Bernevig, Nature (London) **532**, 189 (2016).

[2] A. Alexandradinata, Z. Wang, and B. A. Bernevig, Phys. Rev. X **6**, 021008 (2016).

[3] K. Shiozaki, M. Sato, and K. Gomi, Phys. Rev. B **93**, 195413 (2016).

[4] A. Kitaev, AIP Conf. Proc. **1134**, 22 (2009).

[5] A. P. Schnyder, S. Ryu, A. Furusaki, and A. W. W. Ludwig, Phys. Rev. B **78**, 195125 (2008).

[6] A. P. Schnyder, S. Ryu, A. Furusaki, and A. W. W. Ludwig, AIP Conf. Proc. **1134**, 10 (2009).

[7] C.-K. Chiu and A. P. Schnyder, Phys. Rev. B **90**, 205136 (2014).

[8] C.-K. Chiu, H. Yao, and S. Ryu, Phys. Rev. B **88**, 075142 (2013).

[9] T. Morimoto and A. Furusaki, Phys. Rev. B **88**, 125129 (2013).

[10] X.-Y. Dong and C.-X. Liu, Phys. Rev. B **93**, 045429 (2016).

[11] B. Bradlyn, J. Cano, Z. Wang, M. G. Vergniory, C. Felser, R. J. Cava, and B. A. Bernevig, Science **353**, aaf5037 (2016).

[12] K. Shiozaki, M. Sato, and K. Gomi, Phys. Rev. B **95**, 235425 (2017).

[13] K. Shiozaki and M. Sato, Phys. Rev. B **90**, 165114 (2014).

[14] C. Fang and L. Fu, Phys. Rev. B **91**, 161105(R) (2015).

[15] K. Shiozaki, M. Sato, and K. Gomi, Phys. Rev. B **91**, 155120 (2015).

[16] C.-X. Liu, R.-X. Zhang, and B. K. VanLeeuwen, Phys. Rev. B **90**, 085304 (2014).

[17] M. Ezawa, Phys. Rev. B **94**, 155148 (2016).

[18] P.-Y. Chang, O. Erten, and P. Coleman, Nat. Phys. **13**, 794 (2017).

[19] L. Lu, C. Fang, L. Fu, S. G. Johnson, J. D. Joannopoulos, and M. Soljacic, Nat. Phys. **12**, 337 (2016).

[20] J. Kruthoff, J. de Boer, J. van Wezel, C. L. Kane, and R.-J. Slager, Phys. Rev. X **7**, 041069 (2017).

[21] B. Bradlyn, L. Elcoro, J. Cano, M. G. Vergniory, Z. Wang, C. Felser, M. I. Aroyo, and B. A. Bernevig, Nature (London) **547**, 298 (2017).

[22] B. J. Wieder, B. Bradlyn, Z. Wang, J. Cano, Y. Kim, H.-S. D. Kim, A. M. Rappe, C. L. Kane, and B. A. Bernevig, Science **361**, 246 (2018).

[23] M. Lax, *Symmetry Principles in Solid State and Molecular Physics* (Wiley-Interscience, Hoboken, NJ, 1974).

[24] J. Ma, C. Yi, B. Lv, Z. Wang, S. Nie, L. Wang, L. Kong, Y. Huang, P. Richard, P. Zhang, K. Yaji, K. Kuroda, S. Shin, H. Weng, B. A. Bernevig, Y. Shi, T. Qian, and H. Ding, Sci. Adv. **3**, e1602415 (2017).

[25] A. J. Liang, J. Jiang, M. X. Wang, Y. Sun, N. Kumar, C. Shekhar, C. Chen, H. Peng, C. W. Wang, X. Xu, H. F. Yang, S. T. Cui, G. H. Hong, Y.-Y. Xia, S.-K. Mo, Q. Gao, X. J. Zhou, L. X. Yang, C. Felser, B. H. Yan, Z. K. Liu, and Y. L. Chen, Phys. Rev. B **96**, 165143 (2017).

[26] L. Fu, C. L. Kane, and E. J. Mele, Phys. Rev. Lett. **98**, 106803 (2007).

[27] J. E. Moore and L. Balents, Phys. Rev. B **75**, 121306(R) (2007).

[28] R. Roy, Phys. Rev. B **79**, 195322 (2009).

[29] L. Fu and C. L. Kane, Phys. Rev. B **76**, 045302 (2007).

[30] C. Z. Xiong and A. Alexandradinata, Phys. Rev. B **97**, 115153 (2018).

[31] This deformation argument was first presented in Ref. [3].

[32] M. Cardona and L. Ley, *Photoemission in Solids I* (Springer-Verlag, Berlin, Heidelberg, New York, 1978).

[33] S. Hufner, *Photoelectron Spectroscopy* (Springer, Berlin, 2003).

[34] L. Fidkowski, T. S. Jackson, and I. Klich, Phys. Rev. Lett. **107**, 036601 (2011).

[35] Z. Huang and D. P. Arovas, Phys. Rev. B **86**, 245109 (2012).

[36] Z. Wang, Y. Sun, X.-Q. Chen, C. Franchini, G. Xu, H. Weng, X. Dai, and Z. Fang, Phys. Rev. B **85**, 195320 (2012).

[37] Y. Sun, X.-Q. Chen, C. Franchini, D. Li, S. Yunoki, Y. Li, and Z. Fang, Phys. Rev. B **84**, 165127 (2011).

[38] G. W. Gobeli, F. G. Allen, and E. O. Kane, Phys. Rev. Lett. **12**, 94 (1964).

[39] J. Hermanson, Solid State Commun. **22**, 9 (1977).

[40] D. Pescia, A. Law, M. Johnson, and H. Hughes, Solid State Commun. **56**, 809 (1985).

[41] K. Prince, J. Electron. Spectrosc. Relat. Phenom. **42**, 217 (1987).

[42] G. Borstel, M. Neumann, and M. Wöhlecke, Phys. Rev. B **23**, 3121 (1981).

[43] C. Fang, M. J. Gilbert, X. Dai, and B. A. Bernevig, Phys. Rev. Lett. **108**, 266802 (2012).

[44] M. Atala, M. Aidelsburger, J. T. Barreiro, D. Abanin, T. Kitagawa, E. Demler, and I. Bloch, Nat. Phys. **9**, 795 (2013).

[45] T. Li, L. Duca, M. Reitter, F. Grusdt, E. Demler, M. Endres, M. Schleier-Smith, I. Bloch, and U. Schneider, Science **352**, 1094 (2016).

[46] A. A. Soluyanov and D. Vanderbilt, Phys. Rev. B **83**, 235401 (2011).

[47] R. Yu, X. L. Qi, A. Bernevig, Z. Fang, and X. Dai, Phys. Rev. B **84**, 075119 (2011).

[48] A. Alexandradinata, X. Dai, and B. A. Bernevig, Phys. Rev. B **89**, 155114 (2014).

[49] F. Wilczek and A. Zee, Phys. Rev. Lett. **52**, 2111 (1984).

[50] J. Höller and A. Alexandradinata, Phys. Rev. B **98**, 024310 (2018).

[51] X. Wan, A. M. Turner, A. Vishwanath, and S. Y. Savrasov, Phys. Rev. B **83**, 205101 (2011).

[52] G. B. Halasz and L. Balents, Phys. Rev. B **85**, 035103 (2012).

[53] A. Alexandradinata, C. Fang, M. J. Gilbert, and B. A. Bernevig, Phys. Rev. Lett. **113**, 116403 (2014).

[54] This is distinct from the noncrystalline, $\mathbb{Z}_2$ strong invariant [26,27].

[55] C. L. Kane and E. J. Mele, Phys. Rev. Lett. **95**, 226801 (2005).

[56] In principle we could consider the Kane-Mele invariants $\mathcal{P}_{ij} \in \mathbb{Z}_2$ defined over four time-reversal-invariant planes, which project, respectively, to $ij = 01, 12, 23, 30$. However, given the strong invariant χ^+, only one of the four $\mathcal{P}_{ij}$ is independent. To appreciate this, note that the parity of χ^+ uniquely determines $\mathbb{Z}_2$ strong invariant $\Gamma \in \mathbb{Z}_2$ of 3D time-reversal-symmetric insulators [30]. Precisely, $\chi^+ \bmod 2 = \Gamma$, where $\Gamma = 1$ corresponds to the nontrivial phase. Moreover, Γ is uniquely determined by the Kane-Mele invariants on parallel planes: $\Gamma = \mathcal{P}_{01} + \mathcal{P}_{23} = \mathcal{P}_{12} + \mathcal{P}_{30}$ [47]. Due to g_x and time-reversal symmetries, $\mathcal{P}_{30} = 0$ [30]. Consequently, $\mathcal{P}_{12}$ and $\mathcal{P}_{23}$ are determined uniquely by χ^+ and $\mathcal{P}_{01}$.

[57] R. Roy, Phys. Rev. B **79**, 195321 (2009).

[58] L. Fu and C. L. Kane, Phys. Rev. B **74**, 195312 (2006).

[59] J. Zak, Phys. Rev. B **23**, 2824 (1981).

[60] R. A. Evarestov and V. P. Smirnov, Phys. Status Solidi **122**, 231 (1984).

[61] H. Bacry, Commun. Math. Phys. **153**, 359 (1993).

[62] A. Alexandradinata and J. Höller, Phys. Rev. B **98**, 184305 (2018).

[63] D. Chen, T.-T. Zhang, C.-J. Yi, Z.-D. Song, W.-L. Zhang, T. Zhang, Y.-G. Shi, H.-M. Weng, Z. Fang, P. Richard, and H. Ding, Phys. Rev. B **96**, 064102 (2017).

[64] Any solid that is symmetric under $g_x : (x, y, z) \rightarrow (-x, y + R_2/2, z)$ would also be symmetric under $(x, y, z) \rightarrow (-x, y - R_2/2, z)$, since $(x, y, z) \rightarrow (x, y + R_2, z)$ is also a symmetry of the solid.

[65] J. H. Ryoo and C.-H. Park, Phys. Rev. B **98**, 235403 (2018).

[66] P. J. Feibelman, Phys. Rev. B **14**, 762 (1976).

[67] H. J. Levinson, E. W. Plummer, and P. J. Feibelman, Phys. Rev. Lett. **43**, 952 (1979).

[68] P. J. Feibelman, Prog. Surf. Sci. **12**, 287 (1982).

[69] G. D. Mahan, Phys. Rev. B **2**, 4334 (1970).

[70] These are not symmetries of a spin-orbit-coupled solid.

[71] B. A. Lippmann and J. Schwinger, Phys. Rev. **79**, 469 (1950).

[72] M. Gell-Mann and M. L. Goldberger, Phys. Rev. **91**, 398 (1953).

[73] H. A. Bethe and E. Salpeter, *Quantum Mechanics of One- and Two-Electron Atoms* (Springer-Verlag, Berlin, Goettingen, Heidelberg, 1957).

[74] I. Adawi, Phys. Rev. **134**, A788 (1964).

[75] P. J. Feibelman and D. E. Eastman, Phys. Rev. B **10**, 4932 (1974).

[76] L. L. Foldy and S. A. Wouthuysen, Phys. Rev. **78**, 29 (1950).

[77] E. I. Blount, Phys. Rev. **128**, 2454 (1962).

[78] N. W. Ashcroft and N. D. Mermin, *Solid State Physics* (Thomson Learning, Boston, 1976).

[79] Ψ may be derived by a simple generalization of Adawi's calculation [74] to include the effect of spin. The essential structure of the derivation is identical; one merely has to include a spin-orbit coupling and Darwin terms to V in Eq. (2.1) of Ref. [74] and to interpret ϕ_0 in Eq. (2.3) as a spinor state.

[80] T. Feuchtwang, P. Cutler, and D. Nagy, Surf. Sci. **75**, 490 (1978).

[81] R. Feder, Principles and theory of electron scattering and photoemission, in *Polarized Electrons in Surface Physics* (World Scientific, Singapore, 2013), pp. 125–241.

[82] Because $[H_e, \hat{g}_x] = 0$ and $\hat{g}_x$ is a unitary operator.

[83] D. J. Griffiths, *Introduction to Quantum Mechanics* (Pearson Prentice Hall, Upper Saddle River, New Jersey, 2005).

[84] In practice, this domain may be even smaller due to a short photoelectron escape depth and possibly also the finite cross-sectional area of the photon beam.

[85] In an LEED experiment, an electron beam is directed to and diffracted off the surface of a solid. It is well known [69,74,75] that $\phi_{-\boldsymbol{p}} + G^+ V \phi_{-\boldsymbol{p}}$ is the spinless wave function for an LEED experiment in which the incident electron beam has momentum $-\boldsymbol{p}$; this wave function shall be referred to as an LEED state. In the spinless theory, the inverse-LEED state can be defined as the time-reversed LEED state; time reversal has the effect of inverting momentum $-\boldsymbol{p} \rightarrow \boldsymbol{p}$ and sending $G^+ \rightarrow G^-$, thus producing the spinless analog of Eq. (14). In our spinful theory, the LEED state $(\phi_{-\boldsymbol{p},s} + G^+ V \phi_{-\boldsymbol{p},s})$ describes an incoming, spin-polarized electron beam with momentum $-\boldsymbol{p}$, and the inverse LEED state [right-hand side of Eq. (14)] describes an outgoing beam with inverted momentum ($\boldsymbol{p}$) but the *same* spin polarization s.

[86] B. Ackermann and R. Feder, J. Phys. C: Solid State Phys. **18**, 1093 (1985).

[87] B. Ginatempo, P. J. Durham, B. L. Gyorffy, and W. M. Temmerman, Phys. Rev. Lett. **54**, 1581 (1985).

[88] J. Pendry, Surf. Sci. **57**, 679 (1976).

[89] C.-H. Park and S. G. Louie, Phys. Rev. Lett. **109**, 097601 (2012).

[90] We are describing the physically-motivated scattering geometry in Fig. 6(a), where the sample is finite in all three directions. Rigorously, surface-parallel translations and glide cannot be symmetries of any surface with finite area. Practically, if the sample area is macroscopic, the effect of corners and edges is negligible to a state whose wave function is extended in $\vec{x}$ and $\vec{y}$. Assuming that ψ_i is such an extended state, it may be characterized to a good approximation by the symmetries of a semi-infinite solid (with a single surface); the unitary subgroup of such symmetries is denoted $\mathcal{A}$.

[91] J. Kirschner, Sources and detectors for polarized electrons, in *Polarized Electrons in Surface Physics* (World Scientific, Singapore, 2013), pp. 245–286.

[92] H. Scheidt, M. Glöbl, V. Dose, and J. Kirschner, Phys. Rev. Lett. **51**, 1688 (1983).

[93] J. Kirschner, Surf. Sci. **138**, 191 (1984).

[94] J. Kirschner, D. Rebenstorff, and H. Ibach, Phys. Rev. Lett. **53**, 698 (1984).

[95] J. Kirschner, Solid State Commun. **49**, 39 (1984).

[96] T. Okuda, K. Miyamaoto, H. Miyahara, K. Kuroda, A. Kimura, H. Namatame, and M. Taniguchi, Rev. Sci. Instrum. **82**, 103302 (2011).

[97] T. Zhang, Z. Cui, Z. Wang, H. Weng, and Z. Fang, Phys. Rev. B **101**, 115145 (2020).

[98] For centrosymmetric space groups, distinct glide representations are energy degenerate at each crystal wave vector [2] even in the presence of spin-orbit coupling. Even for noncentrosymmetric space groups, certain other point-group symmetries might result in energy-degenerate initial states that have the same reduced wave vector (k_x, k_y) but belong in distinct glide representations. For example, a reflection symmetry M_z (that inverts z) anticommutes with glide g_x in the spinor representation; hence M_z relates two energy-degenerate states [at $(k_x, k_y, \pm k_z)$] that belong to distinct representations of g_x.

[99] This may be derived from a simple generalization of our theory. Second-order processes are either quadratic in $\boldsymbol{a}\cdot\hat{\boldsymbol{p}}$ or linear in $\boldsymbol{a}^2$, with $\boldsymbol{a} = a_0\vec{y}e^{-i\omega z/c}$ for the parallel alignment and $\boldsymbol{a} = a_0\vec{x}e^{-i\omega z/c}$ for the antiparallel alignment. For either alignment, $(\boldsymbol{a}\cdot\hat{\boldsymbol{p}})^2$ and $\boldsymbol{a}^2$ are invariant under the glide operation, hence the photoelectron has the same glide representation as the initial state.

[100] R. Feder, *Polarized Electrons in Surface Physics* (World Scientific, Singapore, 2013).

[101] J. E. Hirsch, Phys. Rev. B **41**, 6820 (1990).

[102] C. Wu and S.-C. Zhang, Phys. Rev. Lett. **93**, 036403 (2004).

[103] C. Wu, K. Sun, E. Fradkin, and S.-C. Zhang, Phys. Rev. B **75**, 115103 (2007).

[104] A. V. Chubukov and D. L. Maslov, Phys. Rev. Lett. **103**, 216401 (2009).

[105] A. Alexandradinata and J. E. Hirsch, Phys. Rev. B **82**, 195131 (2010).

[106] A. Goldmann, A. Rodriguez, and R. Feder, Solid State Commun. **45**, 449 (1983).

[107] W. E. Spicer, Phys. Rev. **112**, 114 (1958).

[108] C. N. Berglund and W. E. Spicer, Phys. Rev. **136**, A1030 (1964).

[109] T. H. Hsieh, H. Lin, J. Liu, W. Duan, A. Bansil, and L. Fu, Nat. Commun. **3**, 982 (2012).

[110] J. C. Slater and G. F. Koster, Phys. Rev. **94**, 1498 (1954).

[111] C. M. Goringe, D. R. Bowler, and E. Hernández, Rep. Prog. Phys. **60**, 1447 (1997).

[112] P. Lowdin, J. Chem. Phys. **18**, 365 (1950).

[113] A. A. Soluyanov and D. Vanderbilt, Phys. Rev. B **83**, 035108 (2011).

[114] M. V. Berry, Proc. R. Soc. London A **392**, 45 (1984).

[115] R. D. King-Smith and D. Vanderbilt, Phys. Rev. B **47**, 1651 (1993).

[116] M. Taherinejad, K. F. Garrity, and D. Vanderbilt, Phys. Rev. B **89**, 115102 (2014).

[117] N. Marzari and D. Vanderbilt, Phys. Rev. B **56**, 12847 (1997).

[118] A. A. Soluyanov and D. Vanderbilt, Phys. Rev. B **85**, 115415 (2012).

[119] W. A. Benalcazar, B. A. Bernevig, and T. L. Hughes, Science **357**, 61 (2017).

[120] L. Elcoro, B. Bradlyn, Z. Wang, M. G. Vergniory, J. Cano, C. Felser, B. A. Bernevig, D. Orobengoa, G. de la Flor, and M. I. Aroyo, J. Appl. Crystallogr. **50**, 1457 (2017).

[121] Precisely, they are significant near the surfaces of metals or of insulators with surface states (including a wide class of topological insulators).

[122] J. D. Jackson, *Classical Electrodynamics*, 3rd ed. (Wiley, New York, 1999).

[123] We thank Ji Hoon Ryoo for alerting us to this argument.

Correction: A conversion error in Eq. (1) was detected post-publication and has been fixed.